

A calcium imaging large dataset reveals novel functional organization in macaque V4

Tianye Wang^{1-4,*}, Haoxuan Yao^{1-4,*}, Tai Sing Lee^{5,*}, Jiayi Hong¹, Yang Li¹⁻⁴, Hongfei Jiang¹⁻⁴, Ian Max Andolina⁶, Shiming Tang^{1-4,✉}

¹Peking University School of Life Sciences, Beijing, China

²Peking-Tsinghua Center for Life Sciences, Beijing, China

³IDG/McGovern Institute for Brain Research at Peking University, Beijing, China.

⁴Key Laboratory of Machine Perception (Ministry of Education), Peking University, Beijing, China

⁵Center for the Neural Basis of Cognition and Computer Science Department, Carnegie Mellon University, Pittsburgh, United States

⁶The Center for Excellence in Brain Science and Intelligence Technology, State Key Laboratory of Neuroscience, Key Laboratory of Primate Neurobiology, Institute of Neuroscience, Chinese Academy of Sciences, Shanghai, China

*Equal contributions

Correspondence: tangshm@pku.edu.cn

Abstract

The topological organization and feature preferences of primate visual area V4 have been primarily studied using artificial stimuli. Here, we combined large-scale calcium imaging with deep learning methods to characterize and understand how V4 processes natural images. By fitting a deep learning model to an unprecedentedly large dataset of columnar scale cortical responses to tens of thousands of natural stimuli and using the model to identify the images preferred by each cortical pixel, we obtained a detailed V4 topographical map of natural stimulus preference. The map contains distinct functional domains preferring a variety of natural image features, ranging from surface-related features such as color and texture to shape-related features such as edge, curvature, and facial features. These predicted domains were verified by additional widefield calcium imaging and single-cell resolution two-photon imaging. Our study reveals the systematic topological organization of V4 for encoding image features in natural scenes.

Introduction

One striking feature of the primate visual cortex is that neurons with similar stimulus selectivity are organized in columnar structures (Hubel and Wiesel, 1968). Current knowledges of columnar function have come from experiments using small sets of artificial stimuli. Using visual stimuli such as grating, color patch, curvature, and simplified objects, researchers have discovered columns in V1 with selectivity for low-level features such as orientation (Blasdel and Salama, 1986; Hubel and Wiesel, 1968; Ts'o et al., 1990), color (Livingstone and Hubel, 1984; Lu and Roe, 2008), and spatial frequency (Nauhaus et al., 2012), columns in V4 for both low-level (Lu et al., 2018; Tanigawa et al., 2010) and intermediate-level features such as curve and corner (Hu et al., 2020; Jiang et al., 2021; Tang et al., 2020), and columns in IT for high-level features related to objects (Fujita et al., 1992; Tsunoda et al., 2001). Despite these advances, our understanding of the columnar representation of natural images remains limited.

Characterizing columnar representation of natural images requires extensive sampling of the relevant stimulus variations in natural scenes. Since natural images are high-dimensional and complex, without adequate sampling, we might miss the stimulus features and dimensions represented by the neurons. Furthermore, visual features in stimuli are often correlated, without adequate sampling, there will be inferential ambiguity on the true tuning of the neurons (Naselaris et al., 2021).

The recognition of the importance of extensive stimulus sampling has led to several recent studies collecting neural responses to large sets of natural images (Allen et al., 2022; Cadena et al., 2019; Majaj et al., 2015; Stringer et al., 2019; Walker et al., 2019). However, existing primate datasets based on fMRI (Allen et al., 2022) or multi-electrode array recording (Cadena et al., 2019; Majaj et al., 2015) provide minimal information on columnar representation. Here, we used widefield calcium imaging (Seidemann et al., 2016) to achieve long-term stable recording of neural responses at columnar scale in awake monkeys. With this approach, we extensively sampled cortical responses in dorsal V4, an intermediate cortical area in the visual hierarchy. The resulting large dataset contains V4 responses at submillimeter resolution across ten millimeters of the cortical surface to over 17,000 color natural images in three different macaque monkeys.

This dataset contained rich information about neural codes which can be analyzed using machine learning methods (Allen et al., 2022; Bashivan et al., 2019; Ratan Murty et al., 2021; Richards et al., 2022; Ukita et al., 2019; Walker et al., 2019). We used the dataset to train deep neural network models that can accurately predict the cortical response to arbitrary natural images. We then used these models to investigate image feature preferences across the cortex. Combining model predictions and additional experimental verification, we revealed a finely organized V4 cortical preference map. The map contains distinct functional domains preferring a variety of natural image

features, ranging from surface-related features such as color and texture to shape-related features such as edge, curvature, and face components.

Results

A large dataset of macaque V4 cortical responses to natural images

We performed widefield calcium imaging to record V4 cortical responses to a large set of natural stimuli (Fig. 1a). AAVs expressing the calcium indicator GCaMP5G (Chen et al., 2013) were injected into macaque visual cortical area V4. An optical window with a diameter of 10 mm was implanted for imaging (Fig. 1b). During calcium imaging, a 470 nm blue light was used to illuminate the cortex through the optical window, and the green fluorescence signals from the excitation were recorded by a CCD camera (Camera A in Fig. 1a).

To obtain neural responses to thousands of images, we need to integrate recordings across multiple days. We found that continuous blue light exposure causes severe photobleaching resulting in a gradual attenuation of the fluorescence signal (Extended Data Fig. 1). To alleviate this problem and to achieve long-term stable imaging, we developed an intermittent illumination paradigm. A shutter was inserted into the blue light pathway to control the illumination synchronized to the stimulus presentation. During each trial, a stimulus was presented for 500 ms following a 900 ms blank pre-stimulus period while the monkey maintaining fixation. Optical illumination lasting 250 ms occurred twice. One started 150 ms before, and one started 350 ms after the stimulus onset, corresponding to the baseline period before response initiation and the peak response period respectively (Fig. 1c). The fluorescence images recorded in these two periods were used to calculate cortical responses ($\Delta F/F_0$, see Methods). This intermittent illumination method significantly improved the long-term stability of signals (Supplementary Fig. 1). Moreover, we found that the calcium signal was robust between different trials and across days (Fig. 1d), allowing us to integrate data from multiple days into a large dataset. To facilitate multi-day imaging registration, we recorded the blue reflectance images with another camera (Camera B in Fig. 1a) and used the cortical capillaries (Fig. 1b) as the reference for image registration.

We obtained a widefield calcium imaging dataset of visual area V4 of 3 monkeys. Each monkey's dataset consists of a training set for fitting neural network models and a validation set for evaluating the model's prediction performance to novel stimuli. The training set contains single-trial cortical responses to 17,000-20,000 distinct color natural images drawn from the ImageNet dataset (Deng et al., 2009) (see Fig. 1e for examples). The validation set consists of 500 additional natural images, 48 grating stimuli with different orientations and spatial frequencies, and 8 distinct color patches (Supplementary Fig. 2a, see Methods). Each validation stimulus was repeated ten times in random interleave to obtain a more reliable response estimation.

The data of each monkey were collected across 6 consecutive days. To monitor the stability of cortical responses across days during the measurement period, in each recording day we tested 100 natural images selected from the validation set as the fingerprint images. The high degree of correlation of the neural responses to fingerprint images across days confirmed the long-term stability of the measurements for data integration (Supplementary Fig. 3a-c).

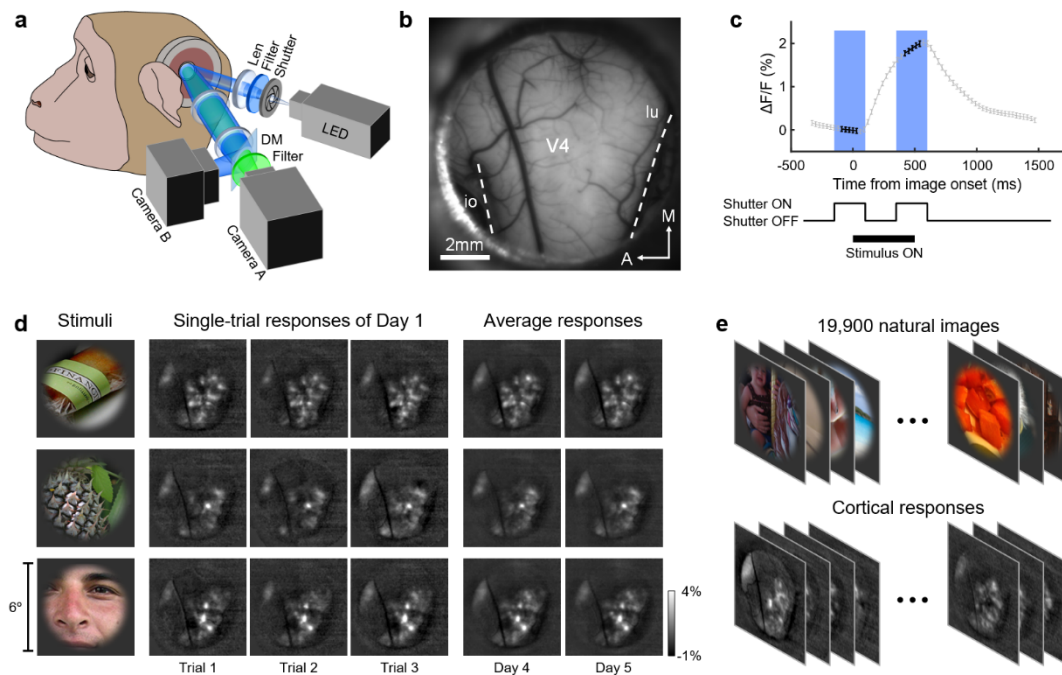


Fig. 1. Widefield calcium imaging of V4 cortical responses to natural scenes. **a**, Schematic of the widefield calcium imaging setup. A shutter was used to control the intermittent illumination. On the detection side, a dichroic mirror (DM 525 nm) splits the reflectance light into green and blue lights, projecting them onto Camera A and Camera B, respectively. **b**, An example of the blue reflectance image recorded by Camera B in V4. A, anterior; M, medial; io, inferior occipital sulcus; lu, lunate sulcus. **c**, Top: Average time course of V4 responses to a stimulus, averaged over the responses to 100 natural images. Blue areas indicate "on" periods of intermittent illumination. Image frames used for computing cortical responses are extracted from the periods indicated by the black labels on the response curve within the shutter "on" periods. Bottom: Control signal for shutter on-off; the black bar denotes the stimulus presentation period. **d**, Example cortical responses to natural images across trials and days. The last two columns show the average responses of 5 repeats on Day 4 and Day 5. **e**, The dataset, used for training the deep neural network, contains cortical responses to 19,900 natural images from monkey C.

DNN modelling of the cortical response dataset

We used the validation set to identify cortical regions that responded robustly to the visual stimuli (Supplementary Fig. 3b, See Methods). We focused our analysis on these

regions and fitted deep learning models to capture the encoding relationship between stimuli and the cortical pixel's responses.

Earlier studies (Cadena et al., 2019; Eickenberg et al., 2017; Guclu and van Gerven, 2015; Ratan Murty et al., 2021; Schrimpf et al., 2020a; Yamins and DiCarlo, 2016; Yamins et al., 2014) suggest that DNNs optimized for object recognition provided the current state-of-the-art model of the primate visual ventral stream. These task-driven DNN's internal representations can be used to fit neural responses to image stimuli via transfer learning. Typically, this is done by fitting the neural responses with a linear transform of feature activations of a specific DNN layer in response to the input image. This feature transfer approach has been shown to produce acceptable response prediction performance, particularly when the training dataset is of modest size (Allen et al., 2022; Cadena et al., 2019; Ratan Murty et al., 2021). However, one drawback of this approach is that data fitting is restricted to the feature space of the pre-trained DNN, and could potentially fail to capture some of the characteristic of the feature space of the brain. One strategy to address this issue is to use the neural data to fine-tune the feature detectors upstream of the selected DNN layer via backpropagation. However, given the large number of trainable parameters in the DNN for recognition tasks, coupled with the modest size of the neural data, such models tend to overfit, resulting in a reduction in generalization performance (Supplementary Table 1). Given these considerations, we proposed a novel neural modelling strategy using knowledge distillation (Gou et al., 2021; Wang and Yoon, 2021) to perform transfer learning (Fig. 2a). Specifically, we used the feature transfer model mentioned above as the teacher to train a student network with much fewer parameter (termed knowledge distillation in machine learning). The student network is then fine-tuned on the targeted neural data again to obtain a final model.

We found this modelling strategy to be very effective in producing a model with superior neural response prediction performance on our measured data (Fig. 2). We trained the feature transfer model with the Add-6 layer of ImageNet pre-trained Xception (Chollet, 2017) (Supplementary Fig. 4a,b). Knowledge distillation was performed by training a small Xception-like DNN (Supplementary Fig. 4c, See Methods) on 100K image-response pairs predicted by the feature transfer model. The prediction performance of the transfer learning model with knowledge distillation (KD Transfer, 73.1% of the achievable performance Fig. 2b) is significantly better than the feature transfer model (Feature Transfer, 68.2%) and the small Xception-like DNN directly training with neural data (Direct, 68.8%). It should be noted that the feature transfer model was better than the directly training model when the amount of data was limited. But this advantage dissipated when the data size reached 17K, as shown in Fig. 2c. On the other hand, the KD Transfer model always maintains its superiority in performance regardless of the size of the training dataset.

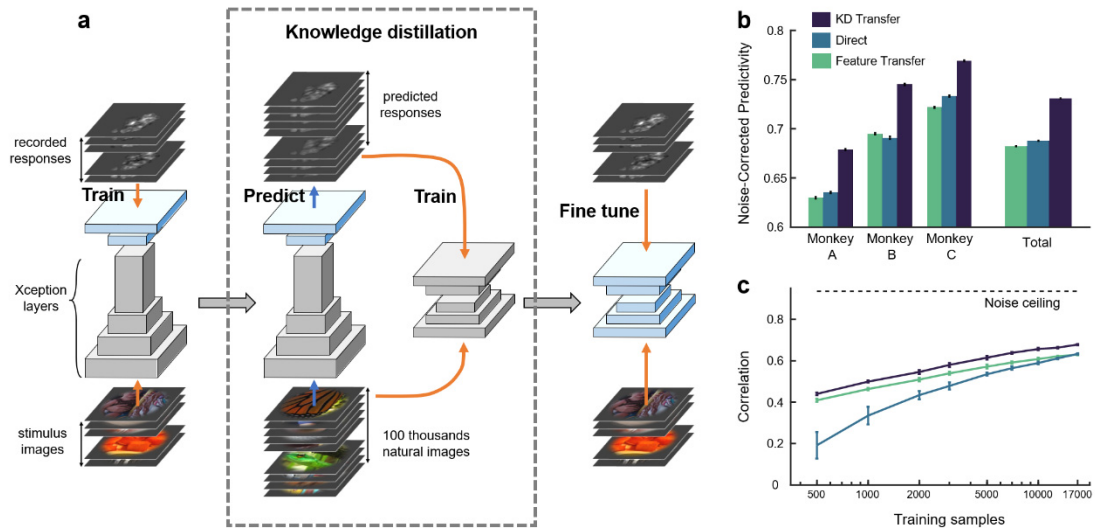


Fig. 2. DNN modeling on cortical response dataset. **a**, Schematic of transfer learning with knowledge distillation. We first used the neural data to train a feature transfer model which uses a two-layer perceptron to map the responses of the Add-6 layer of the Xception to input images to their evoked cortical responses. We then performed knowledge distillation to condense this feature-transfer model to a smaller DNN. This step was completed by training the small DNN using the responses of feature transfer model to 100K natural images. We finally fine-tuned the small DNN on the recorded neural dataset. Parameters of the network layers in blue are optimized on neural data. **b**, Neural Response prediction performance of the feature transfer model (green), the data-driven model (Direct, light blue), and the knowledge distillation transfer model (KD Transfer, dark blue) on the data of 3 monkeys, averaged across all imaged cortical pixels. For each cortical pixel, the performance measure or predictivity of the model is quantified by computing the Pearson correlation between the predicted responses and recorded responses on validation images and then normalizing it with the noise ceiling of the pixel (see Methods, Supplementary Fig. 3d). The error bars denote the SEM. **c**, Performance measured in raw Pearson correlation as a function of training samples relative to the noise ceiling is shown. Plotted lines and error bars indicate mean and standard deviation across results obtained from different bootstrap samples of the data.

Natural image preference maps in V4

The neural network model that can predict V4 cortical responses with high accuracy essentially provides us with a digital twin of V4. This allows us to perform extensive tests *in silico* to dissect and characterize the neural coding in V4 (Abbasi-Asl et al., 2018; Bashivan et al., 2019; Ratan Murty et al., 2021; Ukita et al., 2019; Walker et al., 2019). A classic approach to characterize neural coding is by identifying the optimal stimulus that elicits the strongest response in a neuron or pixel, or region (Bashivan et al., 2019; Ponce et al., 2019; Ratan Murty et al., 2021; Walker et al., 2019). We used our model to search for the optimal stimuli for each cortical pixel through a set of 50,000 natural images. We selected the top 9 images preferred by the model for each location and displayed them in a 3×3 array over that location in cortical surface (Fig. 3a). The

resulting map shows the stimulus preference across the imaged V4 area (Fig. 3b, Supplementary Data). Distinct clusters preferring different types of images were revealed on the map. To characterize the organizational structure of the map, we performed hierarchical clustering to cluster cortical pixels based on the similarity of the top 9 images they preferred. The similarity in image preference between two cortical pixels is computed based on the Pearson correlation between the averaged cortical spatial response patterns to their respective preferred images (Supplementary Fig. 5, See Methods). Hierarchical clustering divided ROI into multiple domains, each showing a preference for natural images with specific characteristics (Fig. 3c, d). Some domains emphasize specific colors, some prefer specific textures, while others emphasize objects of specific shapes, such as round objects or even faces.

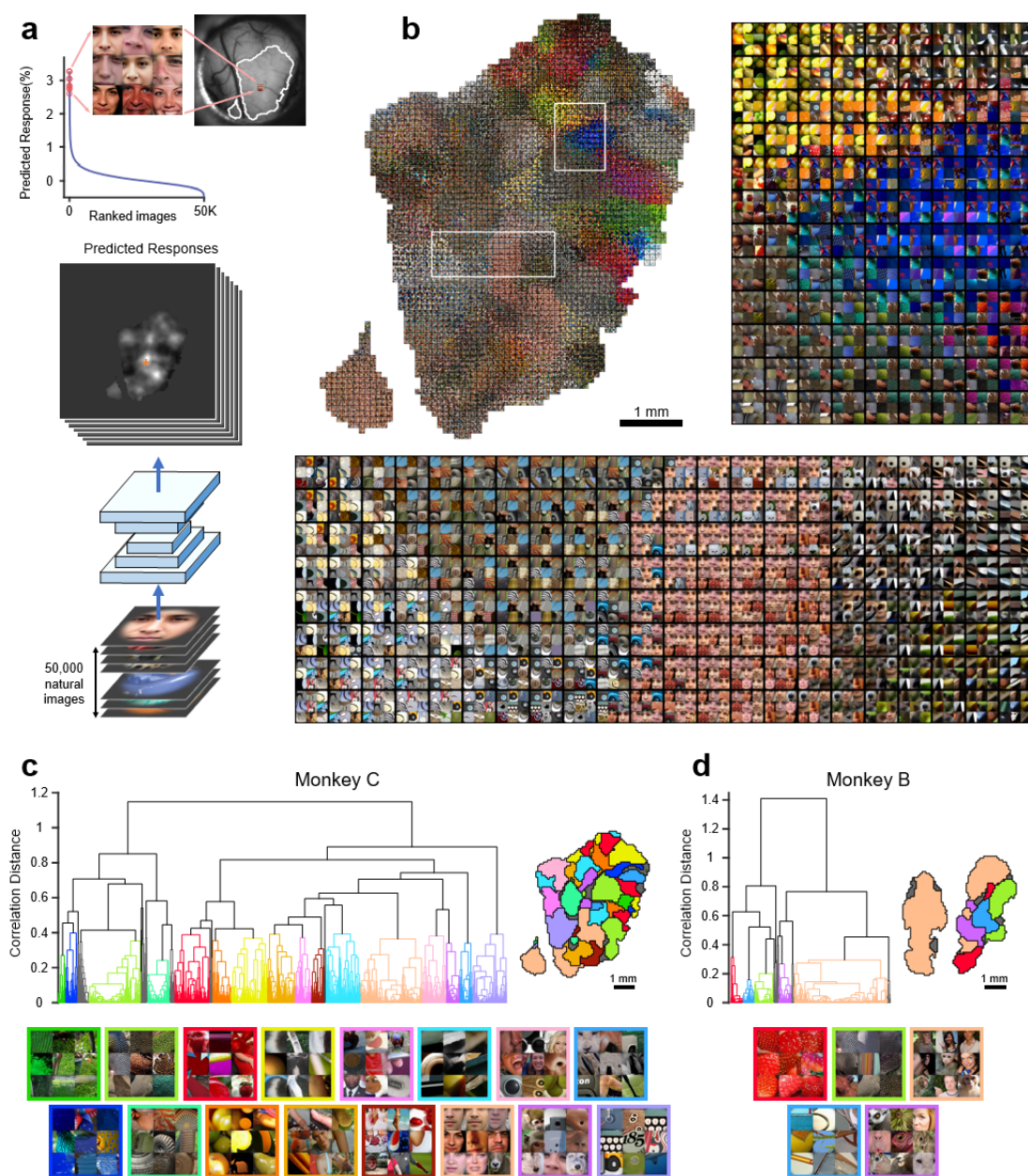


Fig. 3. The natural image preference map predicted by the DNN model. **a**, The synthesis

procedure to generate the preference map. We used the KD Transfer model to predict cortical responses to a 50,000-image set. For each cortical pixel, the top 9 preferred images selected by the model were shown in a 3×3 grid (only the center 4×4 degree of each image is shown here for visualization) at the corresponding imaged cortical position. An example of the top 9 model-predicted images of a cortical pixel, marked by an orange cross, is shown. **b**, The preference map obtained from monkey C. Domains preferring different colors can easily be observed. Zooming into the two regions marked by the white rectangles, we can see cortical pixels preferring distinct shapes and surface attributes. The size of a cortical pixel is 90×90μm. **c**, The cortical pixels in monkey C were hierarchically clustered based on the similarity of the cortical responses to their top 9 preferred images. Clusters that contained connected region with more than 40 pixels were identified as functional domains, marked by distinct color. Clusters that did not meet the above criteria was marked in gray. Left: The dendrogram of the hierarchical clustering. Right: Cortical map with functional domains colored. Bottom: the images predicted to evoke strong responses for the identified domains. The same color scheme, indicating the functional domain categories, is used for the dendrogram, the cortical map and the image frames. **d**, Same as in **c**, for monkey B.

These V4 domains with distinct image preferences were predicted by the model. We next tested these predictions by performing additional widefield calcium imaging on monkey B and monkey C. For each domain, 16 preferred images predicted by the model were selected as test stimuli (Fig. 4a). We found that stimuli selected for different domains elicited distinct cortical responses, and the measured activation patterns were consistent with model predictions (Fig. 4a, b). Fig. 4c shows the responses of each cortical pixel to each group of preferred images associated with the different functional domains (labeled in different color). We found the preferred image group based on their average response is the same as the image group associated the functional domain for 77.9% of the cortical pixels in monkey C and 87.3% of the cortical pixels for monkey B (Fig. 4d). These results indicated that the functional domains revealed by the model-predicted preference map genuinely reflect the organization of image preferences in V4.

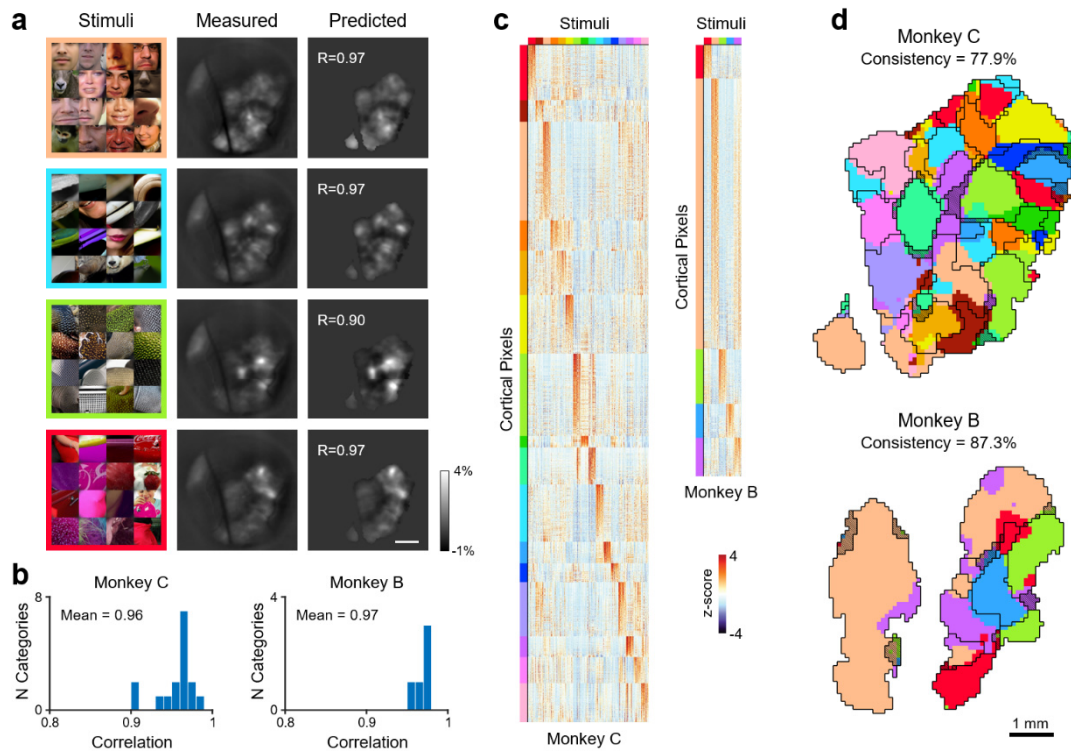


Fig. 4. Experimental verification of the model-predicted preference map. **a**, Test stimuli for the four example domains and their corresponding average activation patterns. The second and third columns show the measured and model-predicted average activation patterns, respectively. R denotes the correlation coefficient between the measured and the predicted pattern. The scale bar denotes 2mm. **b**, Distribution of correlation coefficients between measured and the predicted activation pattern (monkey C: $N=16$, monkey B: $N = 5$). **c**, Population response matrices (z-scored, color scale lower left) to the test stimulus set for all classified cortical pixels (Fig. 3c). Cortical pixels were sorted from top to bottom based on their responses to the test stimuli for their respective category. **d**, Measured stimulus preferences across the ROI. For each cortical pixel, we averaged its response to the test stimuli for each domain and identified the one with the highest response as its preferred category. The color of the cortical pixel represents its preferred category, the black contour outlines the model-predicted domains, and the shaded area represents the unclustered region (as the grey part in Fig. 3c).

Testing single-neuron selectivity on the preference map

Having demonstrated a correspondence between the neural response at the columnar scale and the model-predicted preference map, we next tested the relationship between columnar-scale preference and single-neuron selectivity. We performed a series of two-photon calcium imaging (Li et al., 2017) on ten selected fields of view (FOVs) of monkey C and monkey B respectively (Fig. 5a, b, and Supplementary Fig. 6a). To ensure that the test stimuli could effectively activate the neurons, we used the model to select a set of images preferred by dozens of representative cortical pixels to compose the test stimulus set (see Methods). The

stimulus sets for monkey C and monkey B include 905 and 537 natural stimuli, respectively. We identified soma and dendrites that responded robustly to test stimuli as ROIs for the two-photon imaging analysis (see Methods, Supplementary Fig. 6b). We found that the cortical preferences obtained by widefield imaging are roughly consistent with the stimulus preferences of single neurons in the corresponding region (Fig. 5c, d, f). As shown in Fig. 5c and 5d, the neurons at the face and dot domains also preferred face or dot stimuli. The average tuning of single-cell responses within each FOV is in good agreement with that measured by widefield imaging (Fig. 5e, f). However, single cells (ROIs) exhibited a much greater degree of diversity and sparsity of tuning compared to the FOV responses, indicating that single neurons can encode and discriminate subtler variations of the image features (Fig. 5c, d, f).

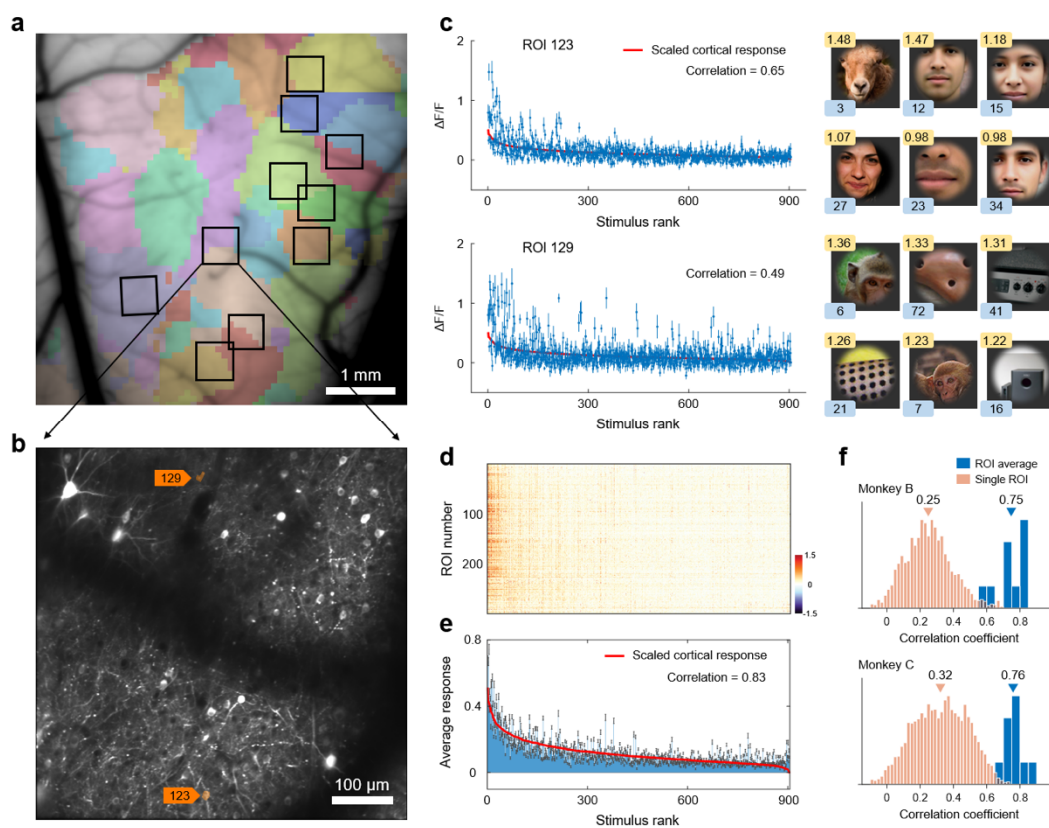


Fig. 5. Stimulus preference testing of single-neurons with two-photon imaging. **a**, Two-photon imaging recording sites in monkey C. The color hue represents the measured cortical preference, following the same color scheme as Fig. 4d. **b**, The two-photon fluorescence image of an example field of view (FOV) averaged over all stimuli, located at the junction of the face and dot domains is shown. **c**, Responses of two example cell ROIs marked in **b** are shown. The error bar represents the SEM. The red line denotes the cortical responses of this FOV measured with widefield imaging. The stimuli are ranked according to the FOV's cortical responses. There is a significant correlation between the response of ROI and FOV, as shown. Stimuli with the top 6 neuronal responses are shown on the right side. For each stimulus, the number on the top left indicates its neuronal response, and the number on the bottom indicates its ranked stimulus index based on widefield imaging. **d**, Population response matrix

of cell ROIs across the FOV region shown in **b**. **e**, Average responses of all ROIs in the FOV region (error bar shows the SEM). As in **(c)**, the red line denotes the FOV's response measured by widefield imaging, rescaled to minimize mean square error with the averaged ROI responses. The correlation between the two is 0.83. **f**, The blue histogram shows the distribution of correlation between the cortical response of each FOV measured by widefield imaging and the average responses of the ROIs within the FOV measured by two-photon imaging. The red histogram shows the distribution of correlation between the cortical response of each FOV and the single ROIs responses within the FOV. Arrows indicate means.

Characterizing feature tuning by feature attribution analysis

Above, we characterized neural coding in terms of natural image preference. However, as natural images typically encompass a mixture of visual features, which specific features in the preferred images that are driving the neural responses remain unclear. To further characterize neural coding in terms of feature tuning, we performed a feature attribution analysis using SmoothGrad-Square (SmoothGrad²)^{38,39} method on our model. For a given input image, this gradient-based algorithm can obtain a heatmap that reflects the contribution of each pixel in the input image to the response of the target cortical region. The heatmap thus highlights the critical features in the image that drive the neural responses. Fig. 6a shows several heatmap examples. For domains preferring dots, edges, and curvature, the critical features highlighted in resulting heatmaps align well with our presumed domain preference. Notably, for identified face domains, the heatmap reveals face components such as the nose and mouth are responsible for driving the neural responses.

We perform an in vivo wide-field imaging experiment to check whether the ablation of the critical features would indeed cause a significant drop in neural response. We targeted the face domain in monkey C and tested 12 sets of images, each derived from an image that was preferred by the face domain. Each set consisted of three test images: the original preferred image, the preferred image with the critical feature masked out, the preferred image with only the critical feature remained (Fig. 6b). The averaged response of the face domain to one set of test images is presented in Fig. 6c. Fig. 6d demonstrates the high consistency between the measured average cortical responses of the face domain and the model-predicted responses to the 12 sets of images (Pearson correlation = 0.84). We found that, although critical features constituted only a small part of the whole image, their occlusion resulted in a greater decrease in face domain's response compared to occlusion of all other parts of the image (Fig. 6e). This evidence suggests that the critical feature revealed by the heatmap is indeed the part of the image critical for driving the response of the target domain.

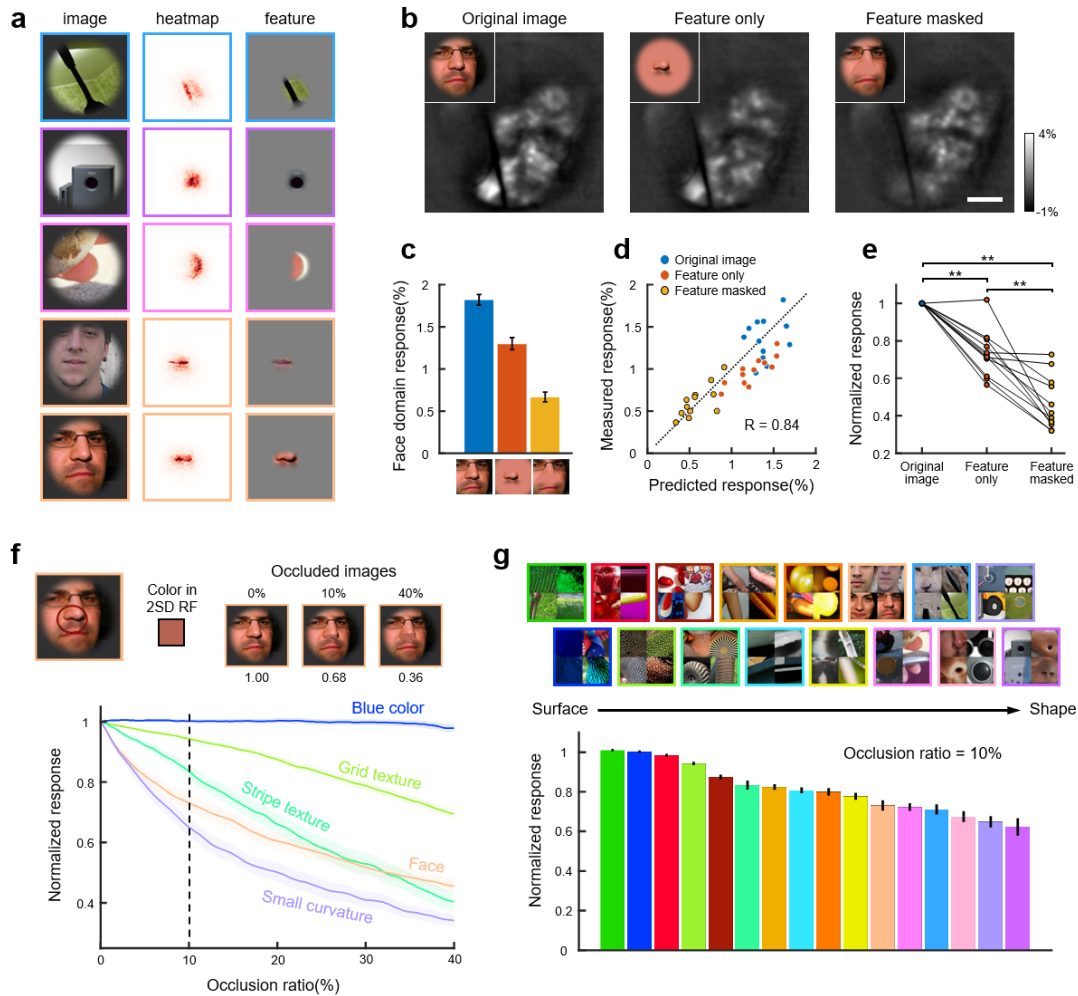


Fig. 6. Using feature attribution analysis to infer critical features for V4 cortex. **a**, Heatmaps of the preferred images highlight the critical features responsible for activating the domains. The first column shows the preferred image for some example domains in monkey C, and the second column shows the corresponding heatmap of each preferred image. The last column represents the image features emphasized by the heatmap. The box colors denote the domain categories. **b**, For the face domain in monkey C, we experimentally tested three types of stimuli – the original preferred images of the domain, images with only critical features visible, and images with critical features masked out. Cortical responses to a set of images are shown. The scale bar denotes 2 mm. **c**, Face domain’s averaged responses to the example stimuli shown in **b**. The error bar represents the SEM. **d**, Face domain’s responses to the 12 sets of stimuli tested, showing a high correlation between the measured and the model predicted responses to the three types of stimuli across the different images. **e**, Comparison of face domain’s responses to the three types stimuli. P-values for a paired t-test are: Original image-Feature only, $4.51e-6$; Original image-Feature masked, $1.95e-8$; Feature only-Feature masked, $1.13e-4$. **f**, Models’ responses to example domains’ preferred images with their critical image regions occluded. Top: For an image preferred by a domain, a fraction of image pixels estimated to be the most important based on the heatmap is occluded with the average color of the image within the 2 SD area of the receptive field (see Fig. 7). A face domain’s preferred

image with 0%, 20% and 40% occlusion and the normalized responses they evoked are shown below. Bottom: The relationship between the occlusion ratio and response for 5 example domains. The solid lines show the mean results of each domain's top 25 preferred images (in the 50,000-image set), and the color shading indicates the SEM. **g**, Average responses of the top 25 images (normalized by the original responses) with their corresponding SEM across different domains at 10% occlusion. Domains that prefer shape attributes exhibit more significant drop in response under small occlusion compared to domains that prefer surface attributes.

We then performed more systematic testing of the stimuli with the critical features occluded for each identified functional domain on the model. For each test image, we used its average pixel color within the receptive field (RF) of the target domain to occlude the critical image region predicted by the heatmap (Fig. 6f). This occlusion eliminates structured image patterns while preserving the average color information of the original image. We gradually increased the size of the occluded region, starting from the pixel with the highest heatmap value and replacing pixels successively in descending order of the heatmap value. We tested the responses of the domain to the preferred image as a function of the proportion of the pixels replaced relative to the domain's receptive field area (Fig. 6f). We found that domains tuned to different features exhibited different degrees of sensitivity to the proportion of occlusion. Under a small proportion of occlusion (10% RF occluded), domains tuned to shape attributes, such as the face domain and the curvature domain, exhibit a more significant response drop than domains tuned to texture and color. This might be attributed to the fact that shape information is usually represented by spatially precise pixels on the contour boundary, while surface features such as color and texture tend to involve large areas of uniform or homogeneous patterns. This difference in response to a small proportion of occlusion can be used as a metric to contrast the feature preference for surface and shape properties. The functional domains could be ordered according to this metric along a surface-shape axis (Fig. 6g, Supplementary Fig. 8). Furthermore, functional domains preferring surface features tend to cluster together on the V4 map, and similarly for functional domains preferring shape features (Supplementary Fig. 8). Such distinct clustering of functional domains might be a principle underlying the topological organization of V4.

The receptive field used in the above occlusion test was derived by averaging the heatmap of many natural images. Specifically, for a target cortical region, we averaged the heatmaps of its top 1,000 images from the 50,000-image set and fitted them with an elliptical Gaussian (Fig. 6b, Supplementary Fig. 7a, b). This method is applicable for estimating receptive fields of cortical regions with various feature preferences. We used this method to estimate the receptive field for each cortical pixel and obtained a fine-scale retinotopic map (Fig. 7b). The average size of the receptive fields exhibited a linear relationship with eccentricity consistent with previous studies (Freeman and Simoncelli, 2011; Gattass et al., 1988; Kolster et al., 2014) (Fig. 7c).

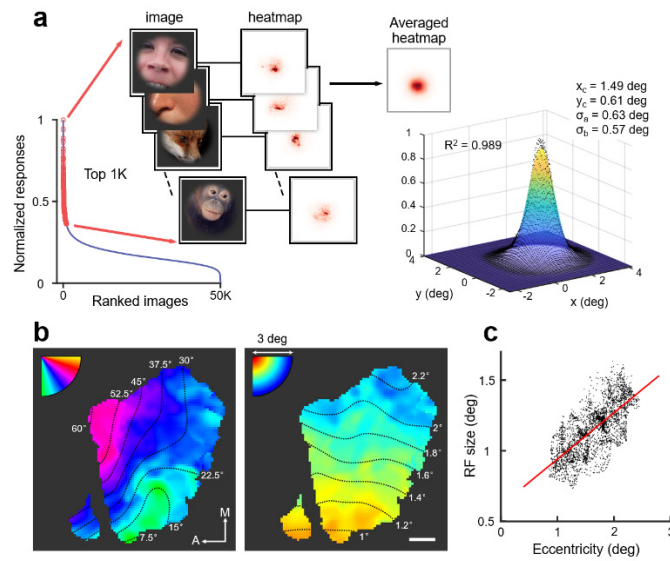


Fig. 7. Estimating receptive field (RF) by averaged heatmap. **a**, Schematic of using heatmap to estimate receptive field (RF). For a target cortical site, we averaged the heatmaps of the top 1,000 images in the 50,000-image set and fitted them with an elliptical Gaussian. **b**, The center location of the fitted elliptical Gaussian was used to estimate the RF position, and the position maps of monkey C in polar-angle (left) and eccentricity (right) are shown. The scale bar denotes 1 mm. A, anterior; M, medial. **c**, The relationship between eccentricity and RF size for all cortical pixels in monkey C, where RF size was estimated by the square root of the area within 1 SD.

Discussion

Using wide-field calcium imaging, we acquired a novel dataset of the cortical response of a large span of visual area V4, at 0.1 mm resolution, to tens of thousands of natural images. We used this dataset to train a deep learning model that can accurately predict the responses of every imaged cortical pixel. This V4 model allowed us to comprehensively characterize the neural tuning of cortical pixels in terms of natural stimuli. Using the model to identify preferred natural images for each cortical pixel, we identified a number of functional domains preferring distinct types of natural images. Further feature attribution analysis revealed that these domains could be arranged along a surface-shape axis based on their feature preferences, ranging from surface properties such as color and texture to shape attributes such as edge, curvature, and facial features.

Digital twin to uncover functional organization in V4

Our deep learning model that can accurately predict neural responses can be considered as a functional digital twin of V4. Using digital twins to characterize neural coding is an emerging research paradigm in visual neuroscience (Bashivan et al., 2019;

Franke et al., 2022; Ratan Murty et al., 2021; Ustyuzhaninov et al., 2022; Walker et al., 2019). This paradigm liberates researchers from a number of normal constraints of neurophysiological experiments, allowing for systematic *in silico* exploration of neural tuning in the high-dimensional image space. There have been several successful applications of this paradigm in the study of the mouse (Franke et al., 2022; Ustyuzhaninov et al., 2022; Walker et al., 2019) and primate (Bashivan et al., 2019; Ratan Murty et al., 2021) visual cortex. Here we combined widefield calcium imaging with the digital twin paradigm for the first time to comprehensively investigate the functional topological organization of the V4 cortex. In contrast to earlier functional organizational studies based on a small number of parameterized stimuli, we used the model to search for preferred images in a large set of natural stimuli, mitigating the possibility of missing meaningful functional domains in the imaged region. Using this approach, not only are we able to reproduce the previously reported functional domains that are tuned to color, orientation (Tanigawa et al., 2010), and curvatures (Hu et al., 2020; Jiang et al., 2021; Tang et al., 2020) we are also able to reveal novel functional domains, such as those preferring facial features and texture.

In addition to predicting *how* V4 would respond to arbitrary images, this V4 digital twin allows us to explore *what* attributes in a given image that are responsible for driving the neural responses using feature attribution analysis. Feature attribution analysis was developed in artificial intelligence to identify the features in the image responsible for a neural network's image classification decision. An occlusion-based feature attribution analysis (Ratan Murty et al., 2021), Randomized Input Sampling for Explanation (RISE) (Petsiuk et al., 2018) has been used to identify the critical features that drive the response of fMRI brain regions. We used an alternative gradient-based approach, called SmoothGrad-Square (Hooker et al., 2019), for heatmap calculation because we found that the mask used in the occlusion-based methods can itself be a feature. For example, zero-value mask is in fact an effective feature for domains preferring black bars. Hence, the occlusion-based methods can potentially give misleading results. Here we used the SmoothGrad-Square method to identify critical features in complex natural images responsible for neural responses. By averaging the heatmaps produced by this method for many natural images, we can obtain an estimate of the receptive fields of the neural units. This novel approach is particularly suitable for mapping the RF of neural units with complex feature selectivity, where traditional stimuli used for RF mapping may be unable to elicit the neural response. Feature attribution analysis also revealed that the feature preferences of the identified domains might lie along a surface-shape axis. A number of earlier studies had reported that V4 neurons were selective for shape (Carlson et al., 2011; Gallant et al., 1993; Nandy et al., 2013; Pasupathy and Connor, 2001; Pasupathy and Connor, 2002) or surface properties (Carlson et al., 2011; Gallant et al., 1993; Nandy et al., 2013; Pasupathy and Connor, 2001; Pasupathy and Connor, 2002). A study on the joint coding of shape and texture (Kim et al., 2019) found that V4 neurons lie along a continuum from strong tuning for boundary curvature of shapes to strong tuning for perceptual texture dimensions. Our results support these ideas and further reveal that

neurons tuned to shape properties and neurons tuned to surface properties are organized topologically in distinct clusters in V4. The strong responses of neurons tuned to surface properties are always driven by spatially dispersed features, while the strong responses of neurons tuned to shape properties are always driven by spatially concentrated features. There is a potential need for separate and specialized neural circuits for computing these distinct feature tunings. Separating the surface and shape processing units into two distinct clusters might facilitate these computations.

Knowledge distillation strategy for creating high performance digital twins

A model that can accurately predict neural responses is crucial for this study. To fully use the large dataset to improve the model performance, we adopted a novel neural modeling strategy based on knowledge distillation. Knowledge distillation is a transfer learning method that compresses a large model and transfers its knowledge to a small one (Gou et al., 2021; Wang and Yoon, 2021). This method enables the fine-tuning of the features of a pre-trained network using neural data, resulting in better performance than earlier methods that used a linear combination of pre-trained features for transfer learning. It would be interesting to further investigate how this knowledge distillation strategy works on modeling neural data from V1, V2, IT; and using other recording methods.

The utility of our widefield calcium imaging dataset

The value of our widefield calcium imaging dataset is not limited to the scientific discoveries reported in this study. Our large-scale, high-quality dataset can be a useful future benchmark for testing and evaluating computational models of the brain. A popular strategy of brain modeling is to develop task-driven artificial neural networks so that their network features can best explain the relationship between stimuli and neural responses (Chang et al., 2021; Choksi et al., 2021; Schrimpf et al., 2020b; Zhuang et al., 2021). The quality and richness of the neural data available in our dataset will allow a reliable evaluation of the competing computational models in terms of neural response prediction and representational similarity. Furthermore, our large dataset also provides spatial organization information of V4, which can also serve as a benchmark for evaluating computational models that explore the principles underlying topographic organization of the primate visual cortex (Blauch et al., 2022; Durbin and Mitchison, 1990; Koulakov and Chklovskii, 2001; Lee et al., 2020).

Future directions

Our study revealed that the functional domains in V4 represent diverse natural image features. The feature preferences of these domains can be organized along a surface-shape axis. The receptive fields of these domains in monkey B and monkey C studied

overlapped considerably and were close to the fovea. The receptive fields of a third monkey were more peripheral. However, our tested images were not large enough to cover the entire receptive fields of neurons in this monkey. Hence, we could not be certain of capturing the complete properties of their neural tunings. Further study is required to elucidate the potential difference in neural codes between the foveal and the peripheral visual fields.

In this study, we have clustered cortical regions based on the similarity of their preferred images. Although images evoke the strongest neural response represent an important aspect of neural selectivity, they do not fully capture the neural tuning functions. Neurons might share the most preferred images and yet different preferences for other images. To fully characterize the functional clustering, it is important to consider their complete tuning functions. This involves analyzing how neurons respond to a wide range of natural images and how they encode the statistical regularities in natural scenes. The accurate digital twin can be useful for such study.

While our two-photon imaging confirmed that the widefield imaging signals correspond to the average neuronal population responses at the submillimeter scale, it also revealed that individual neurons exhibit more complex and diverse selectivity compared to the widefield imaging signals. This suggests that single neurons contain richer and more detailed coding information. A coarse-to-fine approach that uses widefield calcium imaging to first comprehensively characterize the functional map of a cortical region, followed by two-photon imaging to study the detailed tuning properties of neurons in targeted regions, can be an effective strategy for deciphering the neural codes in the visual cortex.

Author contributions

Conceptualization, T.W., T.S.L, and S.T.; Methodology, T.W., H.Y., and S.T.; Software, T.W., H.Y., J.H., and S.T.; Formal Analysis, T.W., H.Y., J.H., and S.T.; Investigation, H.Y. and T.W.; Resources, Y.L., H.J., and S.T.; Writing-Original Draft, T.W., T.S.L., H.Y., and S.T.; Writing-Review & Editing, T.S.L., I.M.A, T.W., and S.T.; Visualization, T.W., H.Y., J.H., and T.S.L.; Supervision, S.T.; Funding Acquisition, S.T.

Acknowledgments

We would like to thank Doris Tsao and Winrich A. Freiwald for their helpful comments and suggestion on the manuscript. We thank the Peking University Laboratory Animal Center for excellent animal care. This work was supported by National Natural Science Foundation of China (grant no. 31730109 and U1909205) and funds from the Peking-Tsinghua Center for Life Sciences. This work was also supported by High-performance Computing Platform of Peking University.

Data and code availability

The data and analysis code will be made publicly available upon manuscript publication.

References

- Abbasi-Asl, R., Chen, Y., Bloniarz, A., Oliver, M., Willmore, B.D., Gallant, J.L., and Yu, B. (2018). The DeepTune framework for modeling and characterizing neurons in visual cortex area V4. *bioRxiv*, 465534.
- Allen, E.J., St-Yves, G., Wu, Y., Breedlove, J.L., Prince, J.S., Dowdle, L.T., Nau, M., Caron, B., Pestilli, F., Charest, I., *et al.* (2022). A massive 7T fMRI dataset to bridge cognitive neuroscience and artificial intelligence. *Nat Neurosci* *25*, 116-126.
- Bashivan, P., Kar, K., and DiCarlo, J.J. (2019). Neural population control via deep image synthesis. *Science* *364*.
- Blasdel, G.G., and Salama, G. (1986). Voltage-sensitive dyes reveal a modular organization in monkey striate cortex. *Nature* *321*, 579-585.
- Blauch, N.M., Behrmann, M., and Plaut, D.C. (2022). A connectivity-constrained computational account of topographic organization in primate high-level visual cortex. *Proc Natl Acad Sci U S A* *119*.
- Cadena, S.A., Denfield, G.H., Walker, E.Y., Gatys, L.A., Tolia, A.S., Bethge, M., and Ecker, A.S. (2019). Deep convolutional models improve predictions of macaque V1 responses to natural images. *PLoS Comput Biol* *15*, e1006897.
- Carlson, E.T., Rasquinha, R.J., Zhang, K., and Connor, C.E. (2011). A Sparse Object Coding Scheme in Area V4. *Current Biology* *21*, 288-293.
- Chang, L., Egger, B., Vetter, T., and Tsao, D.Y. (2021). Explaining face representation in the primate brain using different computational models. *Curr Biol* *31*, 2785-2795 e2784.
- Chen, T.W., Wardill, T.J., Sun, Y., Pulver, S.R., Renninger, S.L., Baohan, A., Schreiter, E.R., Kerr, R.A., Orger, M.B., Jayaraman, V., *et al.* (2013). Ultrasensitive fluorescent proteins for imaging neuronal activity. *Nature* *499*, 295-300.
- Choksi, B., Mozafari, M., Vanrullen, R., and Reddy, L. (2021). Multimodal neural networks better explain multivoxel patterns in the hippocampus. Paper presented at: Neural Information Processing Systems (NeurIPS) conference: 3rd Workshop on Shared Visual Representations in Human and Machine Intelligence (SVRHM 2021).
- Chollet, F. (2017). Xception: Deep Learning with Depthwise Separable Convolutions. 30th IEEE Conference on Computer Vision and Pattern Recognition (Cvpr 2017), 1800-1807.
- Deng, J., Dong, W., Socher, R., Li, L.J., Li, K., and Li, F.F. (2009). ImageNet: A Large-Scale Hierarchical Image Database. *Proc Cvpr IEEE*, 248-255.
- Durbin, R., and Mitchison, G. (1990). A dimension reduction framework for understanding cortical maps. *Nature* *343*, 644-647.
- Eickenberg, M., Gramfort, A., Varoquaux, G., and Thirion, B. (2017). Seeing it all: Convolutional network layers map the function of the human visual system. *NeuroImage* *152*, 184-194.
- Franke, K., Willeke, K.F., Ponder, K., Galdamez, M., Zhou, N., Muhammad, T., Patel, S., Froudarakis,

E., Reimer, J., Sinz, F.H., *et al.* (2022). State-dependent pupil dilation rapidly shifts visual feature selectivity. *Nature* *610*, 128-134.

Freeman, J., and Simoncelli, E.P. (2011). Metamers of the ventral stream. *Nature Neuroscience* *14*, 1195-1201.

Fujita, I., Tanaka, K., Ito, M., and Cheng, K. (1992). Columns for Visual Features of Objects in Monkey Inferotemporal Cortex. *Nature* *360*, 343-346.

Gallant, J.L., Braun, J., and Vanessen, D.C. (1993). Selectivity for Polar, Hyperbolic, and Cartesian Gratings in Macaque Visual-Cortex. *Science* *259*, 100-103.

Gattass, R., Sousa, A.P.B., and Gross, C.G. (1988). Visuotopic Organization and Extent of V3 and V4 of the Macaque. *Journal of Neuroscience* *8*, 1831-1845.

Giovannucci, A., Friedrich, J., Gunn, P., Kalfon, J., Brown, B.L., Koay, S.A., Taxidis, J., Najafi, F., Gauthier, J.L., Zhou, P., *et al.* (2019). CalmAn an open source tool for scalable calcium imaging data analysis. *eLife* *8*.

Gou, J., Yu, B., Maybank, S.J., and Tao, D. (2021). Knowledge distillation: A survey. *International Journal of Computer Vision* *129*, 1789-1819.

Guclu, U., and van Gerven, M.A.J. (2015). Deep Neural Networks Reveal a Gradient in the Complexity of Neural Representations across the Ventral Stream. *Journal of Neuroscience* *35*, 10005-10014.

Hooker, S., Erhan, D., Kindermans, P.-J., and Kim, B. (2019). A benchmark for interpretability methods in deep neural networks. *Advances in neural information processing systems* *32*.

Hu, J.M., Song, X.M., Wang, Q., and Roe, A.W. (2020). Curvature domains in V4 of macaque monkey. *Elife* *9*.

Hubel, D.H., and Wiesel, T.N. (1968). Receptive fields and functional architecture of monkey striate cortex. *J Physiol* *195*, 215-243.

Jiang, R., Andolina, I.M., Li, M., and Tang, S. (2021). Clustered functional domains for curves and corners in cortical area V4. *Elife* *10*.

Kim, T., Bair, W., and Pasupathy, A. (2019). Neural Coding for Shape and Texture in Macaque Area V4. *The Journal of Neuroscience* *39*, 4760-4774.

Kingma, D.P., and Ba, J. (2014). Adam: A method for stochastic optimization. *arXiv preprint arXiv:1412.6980*.

Kolster, H., Janssens, T., Orban, G.A., and Vanduffel, W. (2014). The Retinotopic Organization of Macaque Occipitotemporal Cortex Anterior to V4 and Caudoventral to the Middle Temporal (MT) Cluster. *Journal of Neuroscience* *34*, 10168-10191.

Koulakov, A.A., and Chklovskii, D.B. (2001). Orientation preference patterns in mammalian visual cortex: a wire length minimization approach. *Neuron* *29*, 519-527.

Lee, H., Margalit, E., Jozwik, K.M., Cohen, M.A., Kanwisher, N., Yamins, D.L., and DiCarlo, J.J. (2020). Topographic deep artificial neural networks reproduce the hallmarks of the primate inferior temporal cortex face processing network. *bioRxiv*.

Li, M., Liu, F., Jiang, H., Lee, T.S., and Tang, S. (2017). Long-Term Two-Photon Imaging in Awake Macaque Monkey. *Neuron* *93*, 1049-1057 e1043.

Livingstone, M.S., and Hubel, D.H. (1984). Anatomy and Physiology of a Color System in the Primate Visual-Cortex. *Journal of Neuroscience* *4*, 309-356.

Lu, H.D., and Roe, A.W. (2008). Functional organization of color domains in V1 and V2 of macaque monkey revealed by optical imaging. *Cereb Cortex* *18*, 516-533.

Lu, Y., Yin, J., Chen, Z., Gong, H., Liu, Y., Qian, L., Li, X., Liu, R., Andolina, I.M., and Wang, W. (2018). Revealing Detail along the Visual Hierarchy: Neural Clustering Preserves Acuity from V1 to V4. *Neuron* *98*, 417-428.e413.

Majaj, N.J., Hong, H., Solomon, E.A., and DiCarlo, J.J. (2015). Simple Learned Weighted Sums of Inferior Temporal Neuronal Firing Rates Accurately Predict Human Core Object Recognition Performance. *J Neurosci* *35*, 13402-13418.

Nandy, Anirvan S., Sharpee, Tatyana O., Reynolds, John H., and Mitchell, Jude F. (2013). The Fine Structure of Shape Tuning in Area V4. *Neuron* *78*, 1102-1115.

Naselaris, T., Allen, E., and Kay, K. (2021). Extensive sampling for complete models of individual brains. *Current Opinion in Behavioral Sciences* *40*, 45-51.

Nauhaus, I., Nielsen, K.J., Disney, A.A., and Callaway, E.M. (2012). Orthogonal micro-organization of orientation and spatial frequency in primate primary visual cortex. *Nat Neurosci* *15*, 1683-1690.

Pasupathy, A., and Connor, C.E. (2001). Shape representation in area V4: Position-specific tuning for boundary conformation. *J Neurophysiol* *86*, 2505-2519.

Pasupathy, A., and Connor, C.E. (2002). Population coding of shape in area V4. *Nature Neuroscience* *5*, 1332-1338.

Petsiuk, V., Das, A., and Saenko, K. (2018). RISE: Randomized Input Sampling for Explanation of Black-box Models.

Ponce, C.R., Xiao, W., Schade, P.F., Hartmann, T.S., Kreiman, G., and Livingstone, M.S. (2019). Evolving Images for Visual Neurons Using a Deep Generative Network Reveals Coding Principles and Neuronal Preferences. *Cell* *177*, 999-1009 e1010.

Ratan Murty, N.A., Bashivan, P., Abate, A., DiCarlo, J.J., and Kanwisher, N. (2021). Computational models of category-selective brain regions enable high-throughput tests of selectivity. *Nat Commun* *12*, 5540.

Richards, B., Tsao, D., and Zador, A. (2022). The application of artificial intelligence to biology and neuroscience. *Cell* *185*, 2640-2643.

Schrimpf, M., Kubilius, J., Hong, H., Majaj, N.J., Rajalingham, R., Issa, E.B., Kar, K., Bashivan, P., Prescott-Roy, J., and Geiger, F. (2020a). Brain-score: Which artificial neural network for object recognition is most brain-like? *BioRxiv*, 407007.

Schrimpf, M., Kubilius, J., Lee, M.J., Ratan Murty, N.A., Ajemian, R., and DiCarlo, J.J. (2020b). Integrative Benchmarking to Advance Neurally Mechanistic Models of Human Intelligence. *Neuron* *108*, 413-423.

Seidemann, E., Chen, Y., Bai, Y., Chen, S.C., Mehta, P., Kajs, B.L., Geisler, W.S., and Zemel, B.V. (2016). Calcium imaging with genetically encoded indicators in behaving primates. *Elife* *5*.

Stringer, C., Pachitariu, M., Steinmetz, N., Carandini, M., and Harris, K.D. (2019). High-dimensional geometry of population responses in visual cortex. *Nature* *571*, 361-365.

Tang, R., Song, Q., Li, Y., Zhang, R., Cai, X., and Lu, H.D. (2020). Curvature-processing domains in primate V4. *Elife* *9*.

Tanigawa, H., Lu, H.D., and Roe, A.W. (2010). Functional organization for color and orientation in macaque V4. *Nat Neurosci* *13*, 1542-1548.

Ts'o, D.Y., Frostig, R.D., Lieke, E.E., and Grinvald, A. (1990). Functional organization of primate visual cortex revealed by high resolution optical imaging. *Science* *249*, 417-420.

Tsunoda, K., Yamane, Y., Nishizaki, M., and Tanifuji, M. (2001). Complex objects are represented in macaque inferotemporal cortex by the combination of feature columns. *Nat Neurosci* *4*, 832-838.

Ukita, J., Yoshida, T., and Ohki, K. (2019). Characterisation of nonlinear receptive fields of visual neurons by convolutional neural network. *Scientific Reports* *9*.

Ustyuzhaninov, I., Burg, M.F., Cadena, S.A., Fu, J., Muhammad, T., Ponder, K., Froudarakis, E., Ding, Z., Bethge, M., and Tolias, A.S. (2022). Digital twin reveals combinatorial code of non-linear computations in the mouse primary visual cortex. *bioRxiv*, 2022.2002. 2010.479884.

Walker, E.Y., Sinz, F.H., Cobos, E., Muhammad, T., Froudarakis, E., Fahey, P.G., Ecker, A.S., Reimer, J., Pitkow, X., and Tolias, A.S. (2019). Inception loops discover what excites neurons most using deep predictive models. *Nat Neurosci* *22*, 2060-2065.

Wang, L., and Yoon, K.-J. (2021). Knowledge distillation and student-teacher learning for visual intelligence: A review and new outlooks. *IEEE Transactions on Pattern Analysis and Machine Intelligence*.

Yamins, D.L., and DiCarlo, J.J. (2016). Using goal-driven deep learning models to understand sensory cortex. *Nat Neurosci* *19*, 356-365.

Yamins, D.L., Hong, H., Cadieu, C.F., Solomon, E.A., Seibert, D., and DiCarlo, J.J. (2014). Performance-optimized hierarchical models predict neural responses in higher visual cortex. *Proc Natl Acad Sci U S A* *111*, 8619-8624.

Zhuang, C., Yan, S., Nayebi, A., Schrimpf, M., Frank, M.C., DiCarlo, J.J., and Yamins, D.L.K. (2021). Unsupervised neural network models of the ventral visual stream. *Proc Natl Acad Sci U S A* *118*.

Methods

Animal preparation and surgery

All experimental protocols followed the guidelines provided by the Institutional Animal Care and Use Committee (IACUC) of Peking University Laboratory Animal Center and were approved by the Peking University Animal Care and Use Committee (LSC-TangSM-3). Three adult male rhesus macaques (*Macaca mulatta*) named A, B, and C, aged between 4 and 6 years, were used in this study.

The details of animal preparation for long-term calcium imaging in awake macaque have been described previously (Li et al., 2017). In summary, each animal underwent three sequential surgeries while under general anesthesia. These surgeries involved the implantation of head posts implant, virus injection and the installation of imaging window. During the second surgery, we performed pressure injections of AAV1.hSynap.GCaMP5G.WPRE.SV40 (AV-1-PV2478, titer 2.37e13 GC/mL, Penn Vector Core) at depths of approximately 350 μ m. The injections were carried out at 20-30 locations within V4 visual cortex, with a volume of 100-150 nL per injection. The injection sites were spaced approximately 1mm apart to achieve uniform expression of GCaMP.

Behavioural task

Monkeys were securely restrained using a head fixation apparatus and performed an eye fixation task during image recording. The animal was required to maintain fixation on a small white spot, measuring 0.1° , within a window of 1° for 1.5 seconds to obtain a juice reward. Eye position was monitored with an infrared eye-tracking system (ISCAN) at 120 Hz.

Visual stimuli

Visual stimuli were generated using a ViSaGe system (Cambridge Research Systems) and displayed on a 17-inch LCD monitor (Acer V173, 80 Hz refresh rate), positioned 45 cm away from the subject's eyes. Each stimulus was presented for 0.5 seconds following a pre-fixation period of 0.9 seconds. For each monkey, the receptive field of the imaged region was first estimated with small gratings. In the subsequent experiments, the stimuli were presented over the region's receptive field (Supplementary Fig. 2b).

Stimuli for V4 large dataset. The natural image stimuli used in the large dataset were sourced from ImageNet²⁶, specifically ILSVRC2012 and 8 synsets from the person subtree. The original images were cropped, resized and masked to create round patches measuring 180 pixels (6 degrees) in diameter with soft fade-off.

Our large-scale V4 dataset comprises a training set consisting of neural responses with each image repeated once, and a validation set consisting of neural responses with each image with ten repetitions in random interleave. Each monkey's training set contained cortical responses to over 17,000 unique color natural images. Monkey A, B, and C were tested with 20,000, 17,900, and 19,900 images, respectively, over a period of 4 to 5 days. For validation purposes, a separate set of 500 natural images was used. In addition, the validation stimuli included 48 gratings and 8 color patches (Supplementary Fig. 2a). The 48 gratings comprised 8 orientations (22.5° increments), 3 spatial frequencies (1.0, 2.0, and 4.0 cycles/degree), and 2 phases. The 8 color patches consisted of red, orange, yellow, green, blue, purple, white, and black. The validation sets were acquired over 1 to 2 consecutive days. To assess the image quality and consistency of cortical responses across recording days, we generated a fingerprint stimulus set comprising the first 100 pictures from the validation stimulus set. On days when validation data was not collected, we recorded the cortical responses to these 100 fingerprint stimuli with 5 repetitions. This allowed us to evaluate the consistency of the cortical pixels' tunings as well as their imaging quality.

Stimuli for testing the preference map. The test stimulus set includes preferred images for multiple cortical sites. We manually selected 30 and 50 representative cortical sites with distinct feature preferences for monkey B and monkey C,

respectively. For each site, we used the model's predictions to identify the top 20 images from the 50,000-image set, forming the test stimulus set. We eliminated duplicate images that were selected for different sites, resulting in stimulus sets containing 537 and 905 stimuli for monkey B and monkey C, respectively. Neural responses to these stimuli were recorded using widefield imaging and two-photon imaging techniques. During widefield imaging, the response to each stimulus was measured eight times. In the case of two-photon imaging, the response to each stimulus was measured 6-8 times within each field of view (FOV). To validate the functional domains identified by the model, we selected the model's top 16 predicted images for each domain from the test stimulus set. These images were then used to test the cortical preferences and assess their alignment with the model's predictions.

Stimuli for testing the critical feature. We selected 12 images that were preferred by the face domain of monkey C from the above stimulus set for testing the preference map. For each of these selected images, we computed a heatmap to identify the critical region within the image that drove the response of the face domain. Using Adobe Photoshop, we created two types of images: one in which the critical region was occluded and another in which only the critical region was visible while the rest of the image was occluded. These additional images, along with the original images, formed a test stimulus set comprising a total of 36 images (12 images \times 3 types). We chose a mask color to ensure a smooth transition between the occluded and unoccluded regions. The cortical responses to these stimuli were recorded using widefield imaging, with each stimulus repeated eight times.

Widefield calcium imaging

Widefield imaging setup. We performed widefield calcium fluorescence imaging with a camera imaging system adapted from Imager 3001/M (Optical Imaging). An excitation blue light was obtained with a LED light source (S3000, Nanjing Hecho Technology Co.) passing through a 470/40 nm filter. The reflected light was collected using a pair of lens (Sigma, 50mm) and split into green and blue light with a dichroic mirror (525 nm). The green light was further filtered (525/50nm) and projected onto a green channel camera (Imager 3001/M, Optical Imaging) and was recorded as the fluorescence calcium images at a rate of 33 Hz. The blue light was projected onto a blue channel camera (ZWO ASI533MC Pro, ZWO) and was recorded as the reflectance image at a rate of 20Hz (Fig. 1a). The reflectance image, which captured the blood vessels well, served as the reference for anatomical registration. The imaging focus was adjusted to 300 μ m below the cortical surface. A fast-mechanical shutter was inserted into the blue excitation light pathway to provide intermittent illumination for long-term stable imaging.

Calculating cortical responses. During each stimulus presentation epoch, there were two periods of illumination, each lasting 250 ms. We utilized the fluorescence images recorded during these periods to calculate cortical responses. The first illumination

period commenced at 150ms prior to the onset of the stimulus, while the second illumination period began 350ms after the stimulus onset. We averaged the frames captured during these two periods to obtain the baseline image (F0) and peak response image (F1) respectively. From these images, we computed maps of fluorescence change ($\Delta F/F_0$ map) using the formula $(F1-F_0)/F_0$. To eliminate global signal changes unrelated to the stimulus and to reveal local modulation, we performed a subtraction operation, subtracting a Gaussian blurred ($\sigma=1.0\text{mm}$) version of the $\Delta F/F_0$ map from the original map, resulting in cortical responses that highlight local changes. We found that the cortical responses obtained by this high-pass filtering matched better the responses measured by two-photon imaging as shown in Supplementary Table 2.

Image registration across days. Prior to imaging each day, we carefully adjust the camera system to ensure alignment with the positions on the first day. Our procedure involves focusing on the plane that exhibits the highest sharpness in the blood vessel image. We then laterally moved the camera system to match the vessel image with the reference image acquired on the first day. To assess alignment accuracy, we developed a custom MATLAB software that evaluates image sharpness and lateral position error. Once the alignment is achieved, we move the depth of focus down by 300 μm for recording.

To correct for minor displacement and distortion of the cortex across multiple imaging days, we incorporated additional image correction during data processing. We first aligned the blood vessel image captured by the blue imaging camera with the fluorescence images acquired by the green imaging camera. This alignment involved rotating, rescaling, and translating the blood vessel images. Then, a transformation matrix was generated between the blood vessel images from each day and the reference image acquired on the first day. This transformation matrix was used to correct and align the fluorescence images across days. Since the blood vessel images acquired by the blue channel camera have higher spatial resolution than the fluorescence images, this approach allows us to achieve greater registration accuracy.

DNN Modeling

Data preprocessing for modeling. The stimulus images, initially measuring 200×200 pixels (30 pixels/degree), were resized to 100×100 pixels before being inputted into the model. The raw response map acquired by the camera had a resolution of 512×512 pixels and a sampling rates of 45 pixels/mm, which exceeded the intrinsic spatial resolution of the widefield calcium imaging signal. To simplify the modeling analysis, we rescaled the response maps to 128×128 pixels using bilinear interpolation. We used validation set responses to identify regions exhibiting significant stimulus-related fluorescence changes. Specifically, we conducted one-way ANOVA across responses of 556 validation stimuli, resulting in regions with p-values below 10^{-300} , indicating highly significant changes. These regions were designated as regions of interest (ROIs,

Supplementary Fig. 3b) for modeling purpose. Responses of regions from outside the ROIs were masked to zero during modeling.

Network architecture. Our feature transfer model consisted of a feature extraction and a two-layer perceptron (Supplementary Fig. 4a). The features are the output maps of Add-6 layer of Xception(Chollet, 2017) to a stimulus image. We used the Add-6 layer as its outputs have been demonstrated to be a reliable predictor of V4 responses (see Supplementary Fig. 4b). We used a Keras implementation of Xception, which was trained for the ImageNet classification task. The two-layer perceptron was used to map the features to the corresponding cortical responses. The hidden layer of the perceptron consists of 200 units, designed to extract effective features while avoiding overfitting. To enhance the model's expressive capacity, we incorporate an exponential linear unit (ELU) nonlinearity in the hidden layer. This nonlinearity aids in capturing complex relationships and enhancing the model's ability to represent the data.

The small Xception-like DNN model (Supplementary Fig. 4c) consisted of a CNN encoder that shared architectural similarities with Xception, including depth-wise separable convolution layers and residual learning blocks. The encoder generated nonlinear feature responses from input images. A readout network was used to map the output of encoder to cortical responses. Sigmoid activation function was used to introduce nonlinearity. The encoder converted the RGB input images to $7 \times 7 \times 400$ feature maps, which were fed into the readout network. Each position within the feature maps corresponded to a distinct retinotopic spatial location, containing a column of features, whereas different positions in the imaged V4 cortex encoded different features with similar spatial receptive fields. In order to transform the spatially organized maps of the encoder into feature-organized maps that resembled the organization in the cortex, the readout network first reorganized the input $7 \times 7 \times 400$ spatial-feature map into a $20 \times 20 \times 49$ feature-spatial map. This reorganization swapped the spatial and feature organization. The 400 feature channels were now organized as a 20×20 spatial map, with each column containing that feature channel's responses across various retinotopic locations. This feature-spatial map was then passed through sequences of convolutional and locally connected layers to generate the final response output.

To prevent overfitting, dropout layers with a dropout ratio of 0.1 were introduced to all of the above models, meaning that during training, 10% of the responses were randomly dropped to encourage the model to generalize better to unseen data. Additionally, the feature transfer model utilized an L1 penalty regularization on the connection weights between the hidden layer and Xception features. This regularization encourages sparsity and promotes the selection of more relevant and informative features, reducing the risk of overfitting and improving generalization.

Model training. All the models were optimized using stochastic gradient descent with the Adam optimizer(Kingma and Ba, 2014) and a batch size of 20. When fitting the neural data, models are trained to minimize the mean square error (MSE) on the

training set. To prevent overfitting and ensure the best generalization performance, we used early stopping based on the MSE between predicted and measured neural responses on the validation set. If the MSE failed to decrease during any consecutive 50 passes through the entire training set (50 epochs), the training process would be halted. The model that achieved the best performance on the validation set during the training phase would be saved as the final model. This approach allows us to capture the model's optimal performance while avoiding unnecessary training iteration.

For knowledge distillation, we used the results generated by the feature transfer model as data to train the small DNN model using supervised training. This generated data consisted of image-response pairs derived from 100,000 ImageNet images. The responses were predicted by the feature transfer model that was trained on the neural data. The generated data was split into a training set containing 90,000 images and a validation set containing 10,000 images. We trained the small DNN on this data by minimizing the training set MSE. We also used early stopping based on the MSE on the validation set. The training would be halted if the MSE on the validation set did not decrease in ten consecutive epochs.

Predictivity evaluation. The models were assessed by evaluating the correlation between the predicted responses and the measured responses of each cortical pixel to the validation stimuli. There is an inherent limit to the maximum achievable correlation due to response variability within the same day and across days. To estimate this limit, or noise ceiling, we calculated the correlation (see Supplementary Fig. 3d for statistics) between the responses to the fingerprint stimuli in the validation set and the responses to the fingerprint stimuli averaged across days when the training set were collected. This allowed us to determine the upper bound of correlation that can be achieved considering the inherent variability in the neural responses. The models' achieved correlation is then normalized by the noise ceiling to provide a performance measure.

Preference map analysis

Preference map synthesis. We gathered a set of 50,000 images from ImageNet and prepared them in the same way as we did for generating the stimulus sets used in the experiment. We used the KD Transfer model to predict the cortical responses of these 50,000 images. We then organized the nine most responsive images for each cortical pixel into a 3×3 grid and display it at the corresponding cortical location in the acquired image to derive the preference map.

Hierarchical clustering on the preference map. In the preference map, the preference of each cortical pixel is represented by its top nine images. To cluster these cortical pixels based on the similarities of their preferred images, we employed a method illustrated in Extended Data Figure 5. First, we computed the model's prediction of each cortical pixel's response to the entire set of 50,000 images, and normalized them

to range between 0 and 1. Then, we combined all the pixels' normalized responses to generate a predicted cortical activation pattern associated with each image. We then averaged the activation patterns of the top nine images preferred by each pixel to create the 'cortical response vector' of that pixel. The similarity between two cortical pixels was determined by computing the Pearson correlation between their respective cortical response vectors. This similarity metric enabled us to identify groups of cortical pixels that exhibited similar activation patterns when exposed to their preferred images. To identify functional domains within the V4 cortex based on shared image preferences, we employed hierarchical clustering based on average-linkage, and grouped cortical pixels within a distance threshold of 0.4 (computed as one minus the similarity) into a cluster. Any cluster that included connected regions larger than 40 pixels was considered a functional domain. This approach allowed us to distinguish distinct functional domains within the V4 cortex, based on their collective preference for specific image features.

Two-photon calcium imaging

Two-photon imaging setup. We performed two-photon calcium imaging on monkeys B and C with a Bruker two-photon imaging system (Prairie Ultima IV, Bruker Nano). The wavelength of the femtosecond laser (Insight X3, Spetra-Physics) was set to 1000 nm. Field of views (FOVs) of $600\ \mu\text{m} \times 600\ \mu\text{m}$ were imaged under 1.4 \times zoom with a 16 \times objective (0.8-N.A., Nikon) at a resolution of $1.2\ \mu\text{m}/\text{pixel}$. A fast-resonant scan (30 frames per second) was used to obtain images of neuronal activity. We averaged every two frames, resulting in an effective frame rate of 15 fps. In total, we recorded 20 FOVs, 10 from monkey B and 10 from monkey C, with recording depths ranging from $100\ \mu\text{m}$ to $300\ \mu\text{m}$. To determine the precise position of each FOV relative to the widefield imaging map, we recorded the blood vessel image directly above each FOV as a reference to align the two-photon imaging data with the widefield imaging map.

Data processing for two-photon imaging. We used customized MATLAB code to process the data obtained from the experiments. First, we associated the two-photon image series with the corresponding visual stimuli using the time sequence information recorded by Neural Signal Processor (Cerebus system, Blackrock Microsystems). Then, the images were motion corrected using a normalized cross-correlation-based translation algorithm(Li et al., 2017). This step helped to align the images and mitigate any image shifts caused by motion during recording. For the response to each stimulus, we computed the F0 image by averaging the five frames preceding the onset of the stimulus. Similarly, the F1 image was obtained by averaging the frames from the fifth to the tenth frames after stimulus onset. These F0 and F1 images provided baseline and peak response information associated with a stimulus, respectively. An additional non-rigid motion correction(Giovanucci et al., 2019) was applied to the F0 and F1 images to correct for the cortical deformation during the long recording session.

We used the differential image (ΔF) obtained by F1-F0 to extract regions of interest (ROIs). We averaged the differential images across all repeated trials of the same stimulus. A band-pass Difference of Gaussian filtering (stds of positive and negative Gaussians are 1 and 30 pixels respectively) was then applied to the averaged differential images. The connected subsets of pixels (>30 pixels) with pixel values > 3.5 standard deviations of the mean brightness were selected as ROIs. We further refined the shape of the ROI by calculating the correlation between the ΔF values of the ROI and its neighboring pixels. Pixels with a correlation greater than 0.3 will be assigned to the ROI. Using the above methods, we obtained many overlapping ROIs. To determine whether these ROIs should be merged, we perform hierarchical clustering on the responses of pixels within these ROIs. The pixel response was calculated by $\Delta F/F$ of the ROI to which it belonged. In cases where a pixel belonged to the multiple ROIs, the response was computed as the average of $\Delta F/F$ of those ROIs. We calculated the response of each selected ROI using $\Delta F/F$ and identified visually responsive ROIs by discarding ROIs that did not exhibit significant response selectivity for any of the 537 and 905 test stimuli for monkey B and monkey C, respectively (tested with a one-way ANOVA, $p > 10^{-5}$).

Heatmap analysis

Heatmap synthesis. To produce a heatmap for a specific image of interest and a target cortical region, we employed the SmoothGrad-Square (SmoothGrad2) algorithm^{65,66}. This algorithm relies on computing the gradient map of the model's response with respect to the input image. The SmoothGrad² algorithm operates by introducing Gaussian noise to the image of interest, generating a set of similar images. For each generated image, the model's response is backpropagated to the input of the deep learning model to generate a gradient map, which captures the sensitivity of the model's response to changes in the input. These gradient maps are then squared and aggregated to produce the final heatmap. SmoothGrad² involves two hyper-parameters: σ , the standard deviation of the Gaussian noise, and n , the number of samples to sum over. Here we used $\sigma = 0.2$ (image value $\in [0,1]$) and $n = 20$.

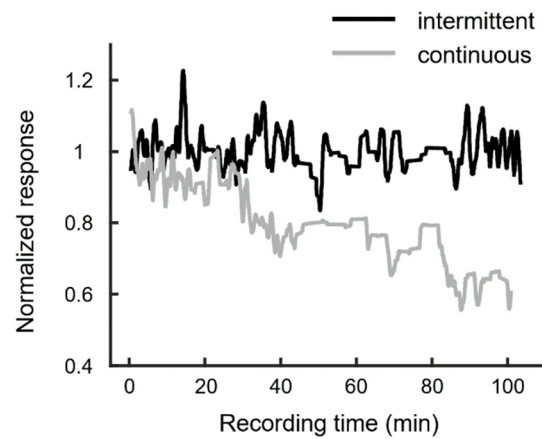
Estimating receptive field. To estimate the receptive field of the target cortical region, we averaged the heatmaps generated from a large set of natural images. Namely, we first calculated the heatmaps for the top 1,000 images in the 50,000-image set for the target cortical region. Next, we normalized the heatmap for each image to ensure that the sum of values on the heatmap equals the cortical response elicited by the image. Finally, we fitted the average of these normalized heatmaps with an elliptical Gaussian:

$$f(x, y) = A \cdot \exp\left(-\frac{x'^2}{2\sigma_a^2} - \frac{y'^2}{2\sigma_b^2}\right) + B$$

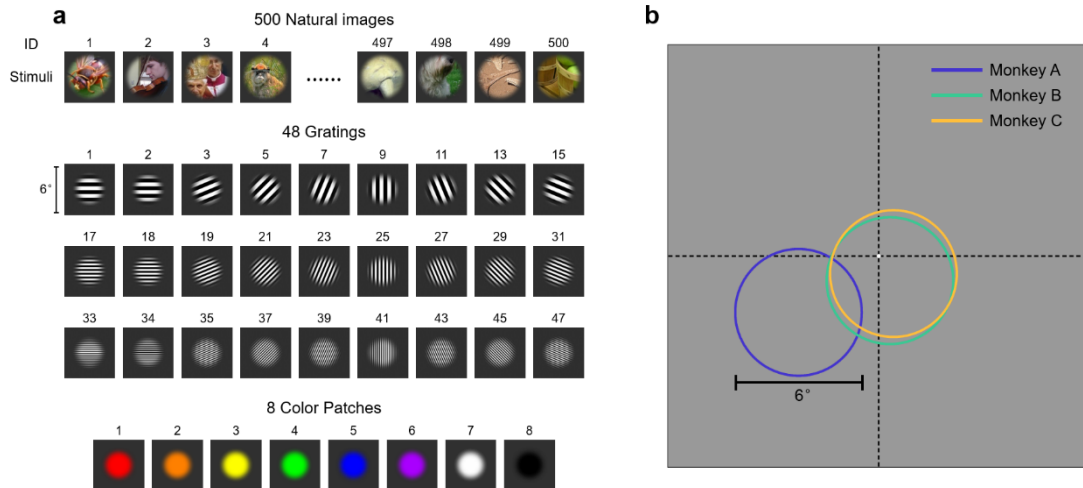
$$\begin{cases} x' = (x - x_c)\cos\theta + (y - y_c)\sin\theta \\ y' = -(x - x_c)\sin\theta + (y - y_c)\cos\theta \end{cases}$$

where A is the amplitude of the Gaussian, B is the offset, σ_a and σ_b are the standard deviations of the elliptical Gaussian along its two principal axes, and x' and y' are transformations of the coordinates x and y , taking into account the angle θ and the offset (x_c and y_c) of the ellipse. In total, there were seven free parameters in the fitting procedure: $A, B, \sigma_a, \sigma_b, \theta, x_c$ and y_c . We define the square root of the area within 1 SD (i.e. $\sqrt{\pi\sigma_a\sigma_b}$) as RF size.

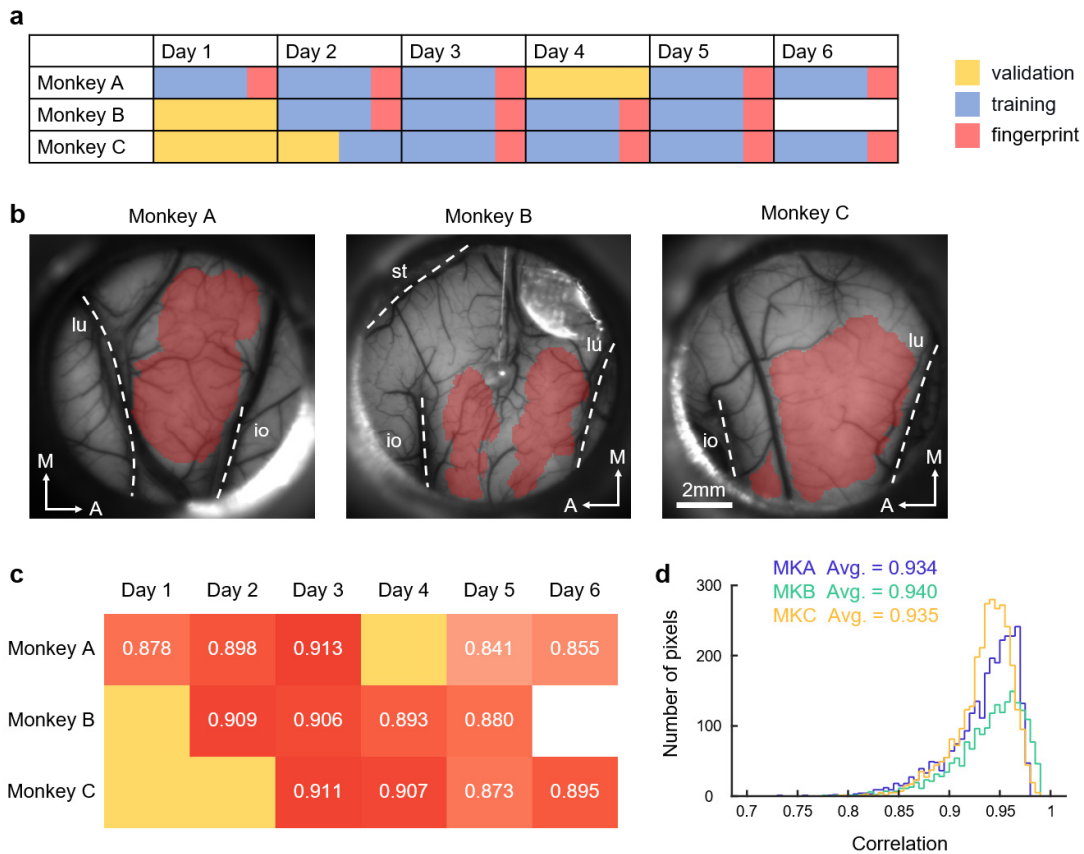
Supplementary Information



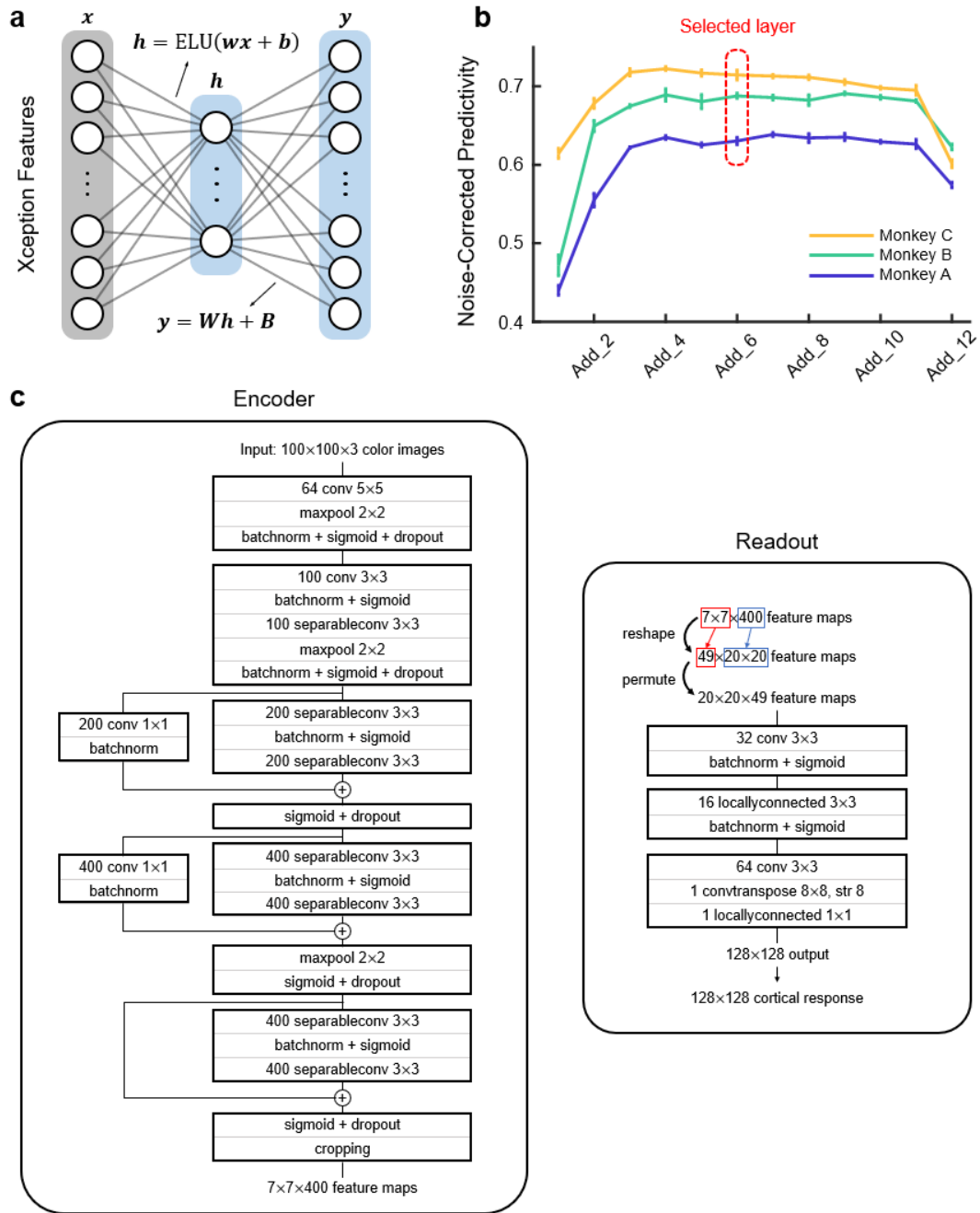
Supplementary Fig. 1. Comparison of photobleaching effect between continuous and intermittent illumination. Cortical responses to 2000 distinct natural images were recorded under continuous illumination (grey line) and intermittent illumination (black line). The average response signal within the ROI exhibited a gradual attenuation under continuous illumination while the response remained stable under intermittent illumination. Both response curves were smoothed with a Gaussian filter (sigma = 10 trials).



Supplementary Fig. 2. Validation images and their presentation regions. **a**, The set of validation images comprises 500 distinct natural images, 48 gratings, and eight color patches. Among the gratings, there are eight orientations (22.5° increments), three spatial frequencies (1.0, 2.0, and 4.0 cycles/degree), and 2 phases. **b**, Stimulus presentation regions for three monkeys. We used small gratings presented at different locations to map the RF region of the imaged cortex. Each monkey had a specific stimulus presentation region chosen to cover its RF. The central white dot indicates the fixation point. For monkey B and monkey C, the RF regions of the imaged cortex were close to the fovea, whereas for monkey A, the RF region more peripheral.

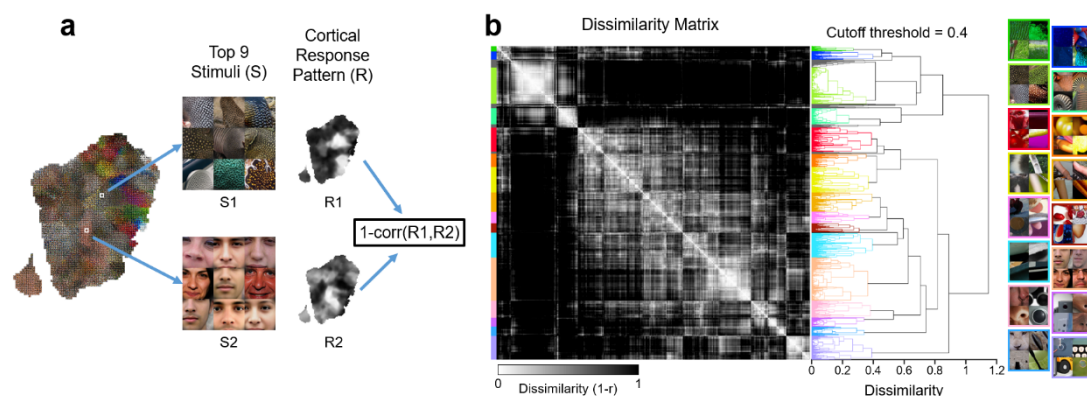


Supplementary Fig. 3. Control the data quality during the imaging period. **a**, The collection schedule of the calcium imaging dataset: The dataset for each monkey was collected over a span of 5-6 days. The validation set (yellow) was recorded on 1-2 consecutive days. During the remaining days, a subset of 100 fingerprint stimuli from the validation set were tested daily to monitor the stability of cortical response. Each of these fingerprint stimuli was tested with 5 repetitions. **b**, Regions of interest (ROIs) were identified by selecting cortical pixels with significant selective responses to the validation stimuli (one-way ANOVA across responses of 556 validation stimuli, $p < 10^{-300}$). The ROIs, highlighted in red, were chosen for subsequent analysis. The anatomical landmarks are labeled as follows: A, anterior; M, medial; io, inferior occipital sulcus; lu, lunate sulcus; st, superior temporal sulcus. **c**, The correlation of cortical responses to fingerprint stimuli across different days. For each cortical pixel within an ROI, the Pearson correlation is computed between average responses (across repetitions) of fingerprint stimuli in the fingerprint session and the validation session. The average correlation for all ROI pixels is shown for each fingerprint session. High correlations (>0.8) indicate that the cortical responses remained stable during the measurement period. **d**, The distribution of noise ceiling of cortical pixel. The noise ceiling is evaluated by computing the correlation between responses of fingerprint stimuli average across all repetitions in all fingerprint session and those in validation session. The colors in the distribution plot represent different monkeys.

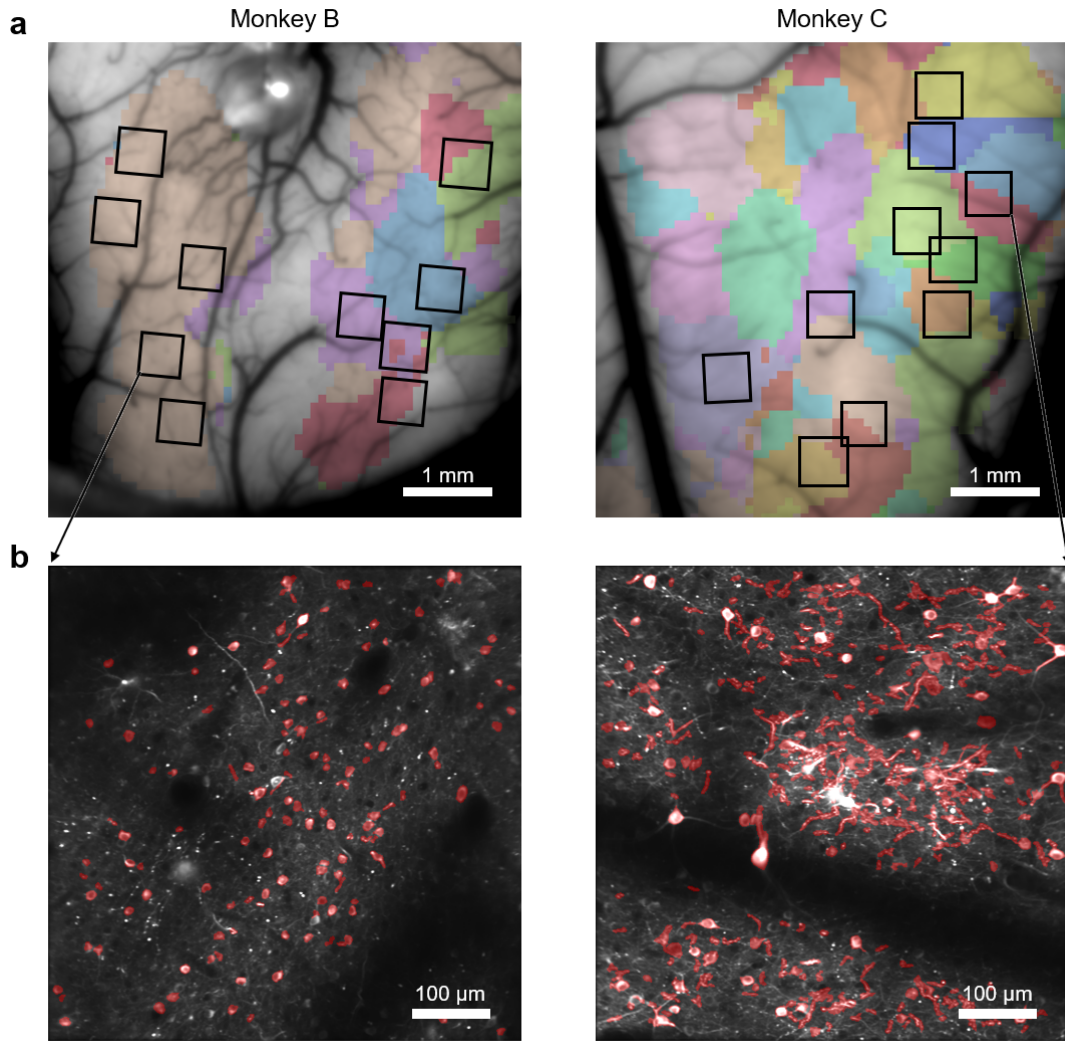


Supplementary Fig. 4. Network design of the neural models. **a**, The network architecture of the feature transfer model utilized a two-layer perceptron to map a Xception layer feature responses (x) to the cortical responses (y). To enhance the expressive power of the model, we applied an exponential linear unit (ELU) nonlinearity to the hidden layer. **b**, Selection of the Xception layer for the feature transfer model. We tested models based on the output layer of each residual block of the Xception, which corresponds to the Add layer. The Add_6 layer (marked by the red box) was selected as it provided a feature map for our feature transfer model that exhibited good performance across all monkeys' data. The error bar represents the standard deviation across different initializations. **c**, The network architecture of the small Xception-like DNN consisted of an encoder and a readout network. The encoder was

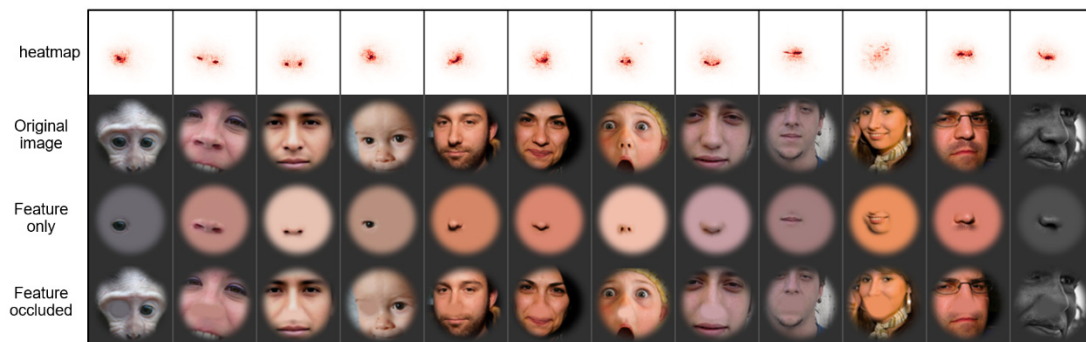
responsible for generating nonlinear features map from input images, while the readout network mapped the feature responses to cortical responses. The encoder shared architectural similarities with Xception, including sequences of convolution layers (indicated by 'conv' with values denoting feature depth and convolution filter size), batch-normalization layers ('batchnorm'), depth-wise separable convolution layers ('separableconv'), max-pooling layers ('maxpool') and residual learning blocks. The readout network transformed the spatially organized maps of the encoder into features-organized cortical response maps. This was achieved by first reorganizing the $7 \times 7 \times 400$ spatial-feature map into a $20 \times 20 \times 49$ feature-spatial map. The map was then passed through sequences of convolution and locally connected layers ('locallyconnected'). Finally, a transposed convolution layer ('convtranspose' with 'str' denoting filter stride) transformed the map into a 128×128 response output.



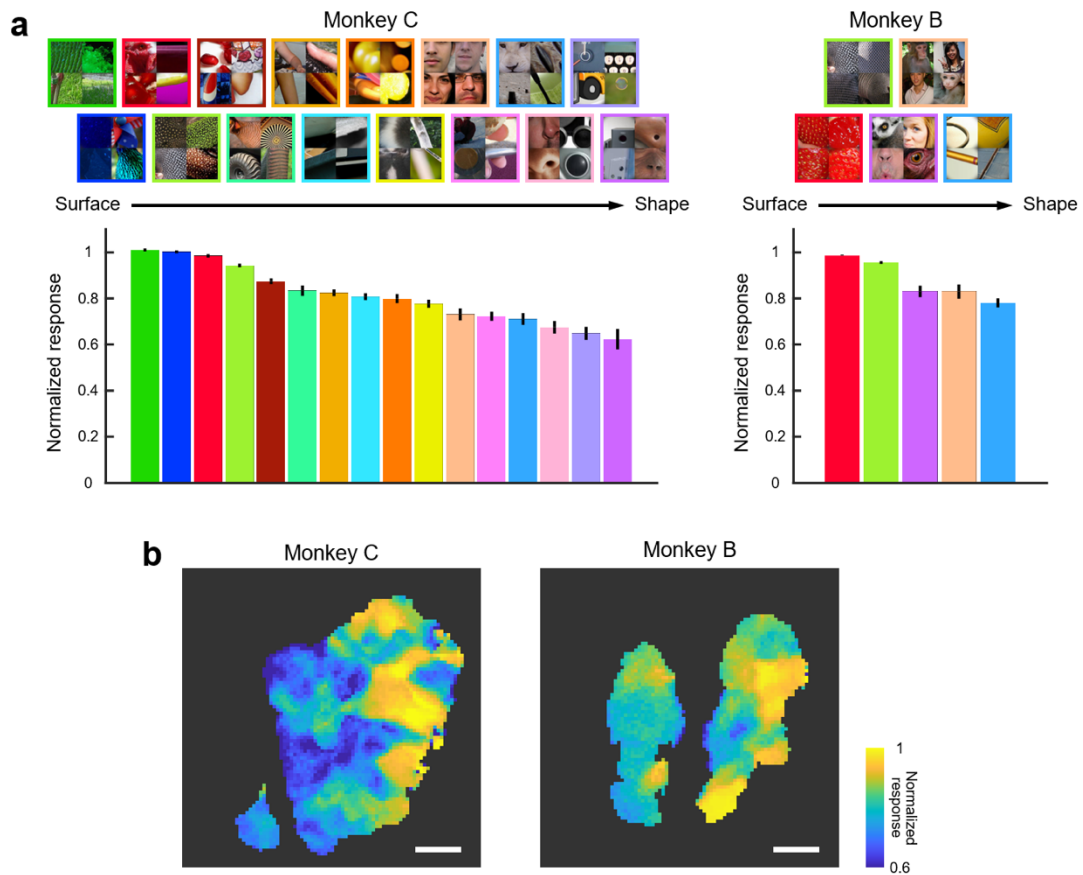
Supplementary Fig. 5. Illustration for hierarchical clustering on preference map. **a**, The similarity distance between cortical pixels is computed as follows. Each cortical pixel's preference is represented by its top nine images. The model-predicted response patterns of these images are averaged, and the dissimilarity between a pair of cortical pixels is computed based on the correlation distance between their response patterns. **b**, Using the dissimilarity measure above, we performed hierarchical clustering to identify the functional domains. Left: The matrix indicates the dissimilarity between pairs of cortical pixels. Pixels were sorted based on their order in the hierarchical clustering. Middle: The dendrogram of the hierarchical clustering process. A cutoff threshold of 0.4 was used to identify the functional domains. Right: The images predicted to evoke strong responses for each identified domain. The functional domains are represented by different colors in the color scheme, which indicates their respective categories.



Supplementary Fig. 6. Two-photon imaging fields of view (FOVs). **a**, The recording sites in monkey B and monkey C. The color hue represents the measured cortical preference, following the same color scheme as in Fig. 4d. **b**, Two example FOVs from monkey B and monkey C. The identified visually responsive regions of interest (ROIs) were marked in red, which included both soma and dendrites.



Supplementary Fig. 7. Stimuli for testing face domain's critical feature. The first row are the heatmaps for the original natural images (second row), the third row are images with only critical features visible, and the last row are images with critical features occluded.



Supplementary Fig. 8. Assessing the cortical feature preference between shape and surface attributes. **a**, Domains preferring shape attributes exhibit a more significant response decrease under small perturbation (rate = 10%). The top shows the preferred images for each domain. The bottom shows the domains' normalized responses to perturbed images. The value and error bar show the average and SEM of each domain's responses to the perturbed images, which are derived from the domain's top 25 images. **b**, Maps for surface-shape preference. For each cortical pixel, preferences between surface and shape features were measured by cortical responses under small perturbation (rate = 10%, as in **a**). The clusters in the maps suggest a potential separate organization of surface and shape features in V4. The scale bar denotes 1 mm.

Model	Monkey A	Monkey B	Monkey C	Total
Fine-tuning	0.638±0.002	0.674±0.002	0.703±0.002	0.672±0.001
Feature Transfer	0.630±0.002	0.695±0.002	0.722±0.002	0.682±0.001
Direct	0.635±0.002	0.691±0.002	0.733±0.002	0.688±0.001
KD Transfer	0.679±0.002	0.745±0.002	0.769±0.001	0.731±0.001

Supplementary Table 1. Noise-corrected predictivity of the cortical response models. The Fine-tuning model and Feature Transfer model share the same network architecture, consisting of feature response computation and a two-layer perceptron readout. The difference between them is that the network weights for generating the feature responses in the Feature Transfer model are fixed, only the parameters of the two-layer perceptron are trained using neural data. In contrast, both the feature extraction and two-layer perceptron are trainable in the Fine-tuning model. The Fine-tuning model initialized the weights of its feature extraction network using the weights from pre-trained Xception. Similarly, the KD Transfer model and the Direct training model share the same architecture. The discrepancy arises in the weight initialization when fitting the neural data. The Direct training model initializes its weights randomly, whereas the KD Transfer model obtains its initial weights through knowledge distillation from the Feature Transfer Model. The reported values and errors in the table represent the average and standard error of the mean (SEM) across all cortical pixels from each monkey.

Filter parameter	Monkey B	Monkey C
$\sigma = 0.2$ mm	0.650±0.036	0.665±0.033
$\sigma = 0.5$ mm	0.709±0.032	0.722±0.027
$\sigma = 1.0$ mm	0.748±0.030	0.759±0.019
$\sigma = 2.0$ mm	0.739±0.032	0.752±0.019
$\sigma = 5.0$ mm	0.739±0.028	0.675±0.025
none	0.727±0.029	0.609±0.028

Supplementary Table 2. Various filtering parameters were tested for calculating cortical responses in widefield imaging. We computed the correlation between the responses of the neuronal population in a two-photon imaging field of view and the responses of the corresponding area in widefield imaging. Our results showed that the optimal filter parameters that yielded the best match between the cortical responses and the neuronal population responses are $\sigma = 1.0$ mm. The reported values and error represent the average correlation and standard error of the mean (SEM) across the two-photon imaging FOVs from each monkey.